Si Quantum Dots for Solar cells

Master's Natural Science Thesis

in Energy Science

Soft Condensed Matter group – Debye Institute

University Utrecht

By

BSc Wingjohn Tang

Supervisor

dr. Marcel Di Vece

August, 2014

Abstract

The solar PV market predominately uses silicon-based solar cell technology, because it is relatively simple to make and for the most part requires only abundant and non-toxic materials. Despite much research into new solar cell concepts and use of other materials, silicon is still the most attractive material of choice. A promising new concept for solar cells that can be combined with silicon, utilizes a class of nanomaterials that are named quantum dots. Their small dimensions of a few nm have the consequence of spatial confining the particles, with two special properties as a result. The first is the tuneable band gap, which makes it interesting for use in tandem solar cells to reach even higher efficiencies. The second is the direct-like band gap for silicon that significantly increases the light absorption, paving the way for thin-film silicon based solar cells that save material costs.

This research was focused on investigating silicon nanoparticles produced with a gas phase aggregation cluster source Depositions were done on various substrates and characterisation of the nanoparticles was performed with multiple techniques like transmission electron microscopy, Raman spectroscopy and time resolved photoluminescence spectroscopy. Different stages of silicon nanoparticle formation were observed for certain tuneable parameters of the cluster source. 'Cauliflower'-like particles of about 50-100nm were found, that were composed of smaller silicon nanoparticles. It is thought that the former are an intermediate stage towards the formation of crystalline particles. Both photo luminescence and UV-Vis photo absorption results show that they consist of small crystalline and amorphous distinct regions. The amorphous silicon provided a strong signal due to its direct band gap. No quantum confinement effects were observed, which might be because the distance between the nm-sized crystalline regions are too close. The optical and structural characteristics of 'cauliflower' particles were investigated in this work and created more insight to apply the cluster source to produce silicon nanoparticles for solar PV.

Table of Contents

1. Introduction

Background and state of research

Solar cells (or Photovoltaic (PV) cells) are a group of engineered devices made to generate electricity directly from sunlight. What was once largely driven by development for its use in space decades ago, is now being developed for terrestrial use.[1] The devices based on bulk crystalline silicon (c-Si) currently dominate the commercial solar PV market. The total of this added up to 90% of total solar cells production in 2008, counting both mono- and polycrystalline silicon solar cells. Mono-crystalline Si is a material that consists of a large homogeneous single Si crystal with an ordered structure. Polycrystalline Si in contrast, is a heterogeneous material formed by numerous crystallites with a disordered structure. The solar cell installation in 2008 amounted to 7.9 GW peak power and more recently, 36.9 GW peak power in 2013. Over the years the production has seen a steady annual growth of about 40%. Yet the total power generated that year was less than 0.1% of the total world's electricity production in 2008.[2] An expected percentage of 0.85% of electricity demand will be produced worldwide by solar PV in 2014.[3] C-Si solar cells have the advantage of several key improvements that give it the highest efficiency on the market. These focus on minimizing 1) photon, 2) carrier and 3) electrical losses by 1) roughening up the front surface with acid etching, 2) SiO_2 passivation of back surface, 3) Selective emitter, respectively to name some examples.[4] The highest efficiency reached with lab-made c-Si solar cells is 25%. The efficiency offered by the best industrial devices is 16-18%, which is a large efficiency difference, because of the limitations posed by economic factors.[5] Note that 25% comes very close to the maximum theoretical efficiency for a c-Si solar cell which is 30% (Shockley-Queisser limit). For solar PV to become competitive with coal and natural gas however, further production cost reductions ($/watt) are needed (e.g. thinner wafers for polycrystalline Si), as high efficiency lab-made solar cells does not necessarily translate to lowered costs of production. Improvements that are introduced in the industry should increase conversion efficiency without sacrificing automation, high cost of materials and a low production speed.[6]

Figure 1 shows two solar cells, one based on mono c-Si and the other one based on poly c-Si. The lower scheme shows the cross-section of a mono c-Si solar cell. It is basically a semiconductor diode, consisting of a single semiconductor p-n junction where electrons are excited under illumination in the n-doped region on one side, leaving a hole. It is also called the electron producing side. The electrons (majority charge carriers) experience an electric field and travel across junction and into the p-doped silicon side. This is the electron accepting side where there are free holes (majority charge carriers). The holes travel the opposite direction of the electrons. The aforementioned electric field is created by a region near the p-n junction called the depletion zone. N-doped semiconductor have mobile electrons with positively charged atoms called donors, that when it is connected with a p-doped semiconductor containing mobile holes and negatively charged atoms, electrons near the junction will experience a concentration difference across the boundary and will flow to the bulk of the p-region. Vice versa for holes. The absence of these mobile charge carriers in this once charge-neutral region near the junction thus means it develops a charged region called the depletion zone (see figure 2).[7] This allows electrons to flow in only one direction and reach the electrical contacts. The back surface field reduces the recombination of minority charge carriers (the electrons), which would otherwise negatively impact conversion

efficiency.[8] After the electrons are conducted through the series of electrical contacts, they are able to recombine with the holes. [9]

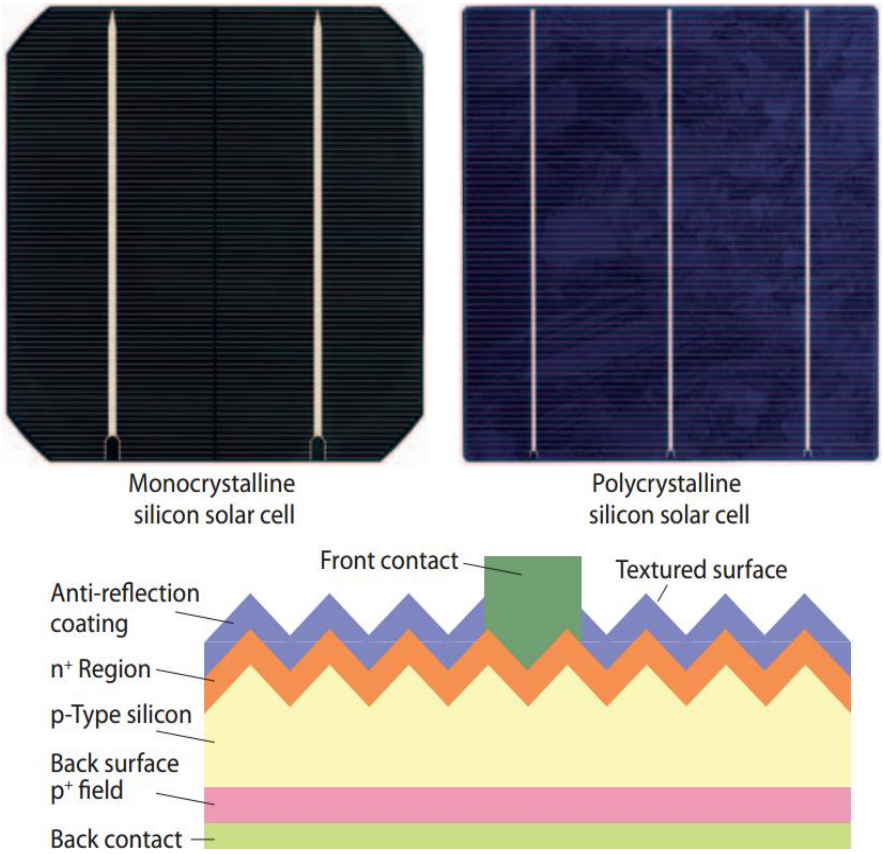

Figure 1) Upper two photos show monocrystalline and polycrystalline silicon solar cells, while the bottom scheme shows a monocrystalline solar cell cross-sectioned and simplified.

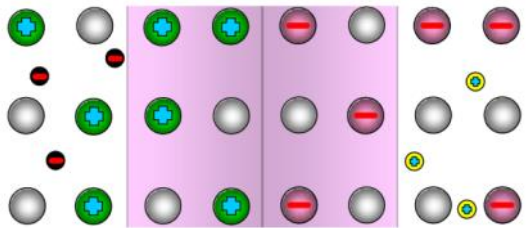

Figure 2) P-n junction depicting charge depletion zone (purple) devoid of free electrons and holes. Donor (green) and acceptor (purple) atoms thus form a charged zone and this produces an electric field.

Thin film solar cells

Another type of solar cells is based on thin film technology which are made by depositing a few µm thick layer of photovoltaic material on a substrate, for example, amorphous Si (a-Si) or Copper Indium Selenide (CIS) through a process called plasma enhanced chemical vapour deposition. Since its more recent market introduction it has accounted for about 10% of the market share, in part thanks due to its smaller profile and flexibility that allows it to be placed on buildings where c-Si solar modules could not be placed. c-Si is a weak absorber of light compared to the stronger light absorbing active material in thin film solar cells. That is why c-Si solar cells need thicker wafers of a few hundred µm. However, thin film solar cells have a lower efficiency (highest 8-9%), because overall the thin film solar cells absorbs less light.[10] This requires techniques that enhance its light absorption which increases the so called effective absorption length.[11] There are several advantages to thin film solar cells, one of which is the high potential in reducing the costs of production. This is thanks to its savings in active materials, but also due to lower temperature manufacturing conditions for a-Si as an example[12], and automation (flow through, instead of batch process).

Research motivation

Motivations for research on the newest generation of solar cells focus on improving efficiency of thin film solar cells and use of abundant materials that are also environmentally-friendly. Examples of emerging solar cell technologies are quantum dot solar cells (QD-SC) and dye-sensitized solar cells (DSSC). These ideas offer promising cost reduction of solar PV modules. Through research, the technology could reach the stage of maturity by offering the same competitive price of electricity production by coal or gas using abundant materials. This would incentivise governments, companies and likewise consumers for solar energy. At the same, subsidies for promoting solar cells will no longer be needed. Avoiding the use of fossil fuels will reduce greenhouse gasses emissions, decrease reliance on the limited fossil fuel supply and secure energy security in the future, while avoiding harmful emissions like SO_2, fine dust and heavy metals such as mercury. Lastly, the scientific community will benefit as they have the opportunity to study novel solar cell configurations and this opens up investigations for further improvements.

Quantum Dot solar Cells

A class of nano-materials called quantum dots (QDs) has a lot of potential for seeing use in photovoltaic cells. These semiconductor nano-crystals in proposed cell configurations have been shown by researchers to have theoretical efficiencies over 60% by increasing the photo voltage or the photo current output. The theoretical efficiency is more than double the Shockley-Queisser limit for a c-si solar cell. Experimental results have yet to demonstrate the increased efficiency to date however and to also achieve stable QD-SC.[13] QDs have a typical size range in of a few nm. They have an advantageous property where they can be selectively tailored-made to absorb photons for different regions of the solar spectrum and emit photons of longer wavelengths by only varying the size of the particle. This is in contrast to the bulk material. When a photon with energy larger than the band gap excites an electron from the ground to a higher state, a hole is also produced. The band gap is the energy gap between the conduction and valence band of a semiconductor. An exciton i.e. a hole and an excited electron, experiences spatial confinement in all 3 dimensions in a QDs compared to the space in the bulk

semiconductor material.[14] This is due to the onset of strong quantum mechanical effects which places QDs as a material between individual atoms and bulk semiconductors. Each QD consists of hundreds to thousands of atoms,[15] which means the energy levels near the edges of the conduction and valence band are more discrete due to a limited amount of energy levels. The same bands in bulk semiconductor are continuous. The change of the energy structure results in the band gap energy becoming larger with decreasing dot size (see figure 3b). [16] Figure 3a shows one schematic of a solar cell that uses CdS QDs and TiO_2, that has reached an efficiency of ~10 percent with still room for improvement.[17]

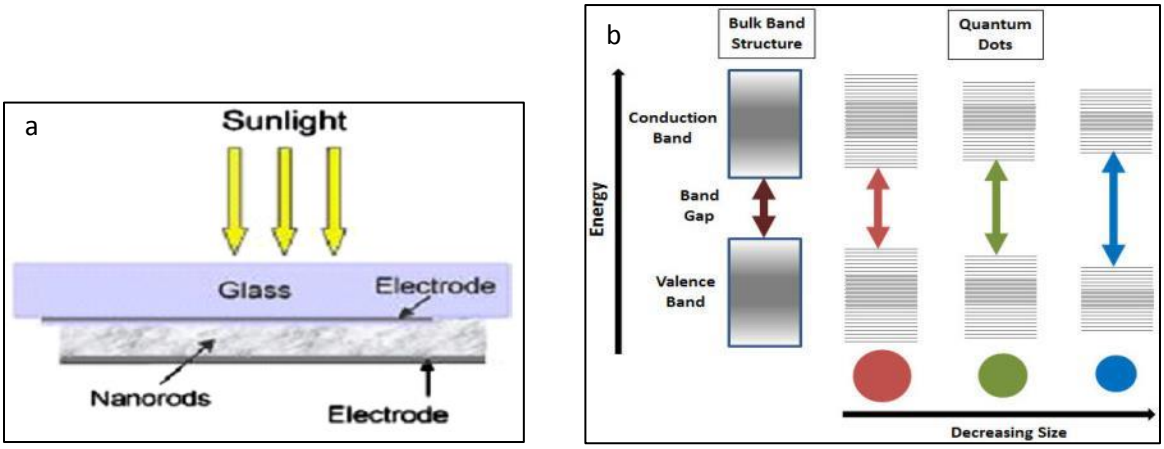

Figure 3a) Scheme of a solar cell based on QD/nanowire, that form nano-rods. (b) Conduction and valence band for bulk semiconductor material and illustration of discretization of the conduction and valence band for quantum dots with decreasing dot size and change of the band gap energy.

Microcrystalline silicon, amorphous silicon, nano-crystalline silicon (µc-, a-, nc-Si)

Some important differences are discussed between the different mc-Si, nc-Si and a-Si phases in this section. a-Si or amorphous silicon is characterized by a disordered network of mostly tetrahedral bonded Si with presence of Si atoms that are only covalently bound to three neighbouring Si atoms. The position of the remaining, uncoordinated bond of these Si atoms is called a dangling bond and is also the main source of defects. The bond lengths and the angles between bonds differ from an ordered, crystalline Si lattice which results in weaker and less stable Si-Si bonds.[18] To reduce the number of defects in a-Si, hydrogen is used to terminate the dangling bonds to obtain a-Si:H for use in solar cells. This also introduces the unwanted Staebler-Wronski effect. It lowers the conversion efficiency of a-Si:H thin film solar cells. The explanation for this is a reduced photocurrent when it is exposed to light overtime. The breaking of the relatively weak Si-H2 bonds and the subsequent re-emergence of the defects act as recombination centres for excited electrons and are responsible for this performance degrading phenomenon.[19,20]

µc-Si:H, or rather hydrogenated microcrystalline Si, consists of crystallites of about 10 to 50 nm big. µc-Si:H is a heterogeneous material of which the crystallites can be fixed in an a-Si phase, or they can be separated by grain boundaries that are small, transition regions (also called grains) and contain defects that are reduced by adding hydrogen. These would otherwise hinder electron transport and render it

less suitable as the active material in solar cells. It has properties similar to c-Si like an indirect band gap and a lower absorption of UV/visible light than a-Si:H, so it requires a comparatively thicker layer. On the other hand, μc-Si:H absorbs more of the near IR light made (partly) possible by light scattering through its rough film surface, which makes it useful as the bottom cell in a stacked solar cell configuration. Here, it absorbs photons of lower energy transmitted by the upper cell(s), e.g. with a-Si:H as the active material that absorbs higher energy photons.[21] The advantage over the use of a-Si-H in solar cells, is that μc-Si:H thin film solar cells generally do not show the Staebler-Wronski effect. It is noted that μc-Si:H is a term for the different hydrogenated microcrystalline Si phase types that come in various microstructures, forms and crystallite orientation. It can also coexist with the a-Si phase, so each prepared Si layer from the same or different synthesis technique may produce another crystalline/amorphous ratio (volume fraction). An additional feature for microcrystalline Si is that when it is grown on a substrate, the degree of crystallization is higher up in the layer than down close to the substrate. Depending on the crystalline fraction of the μc-Si:H in question, it may be possible that degradation from the Staebler-Wronski effect still occurs. [22]

A more serious factor that negatively influences μc-Si:H is post-oxidation. Exposure to air overtime changes its electrical properties (conductivity and transport) in a manner of weeks. This long-term stability problem is not seen when the μc-Si:H layer is incorporated into solar cells however, presumably due to hermetic sealing. The stability against oxidation could be better in μc-Si:H where fewer cracks are present, and the crystallites are packed together in a more compact manner. Figure 5 shows a TEM picture of a-Si:H and μc-Si:H phases grown on ZnO.[23] At the bottom near the substrate exists an amorphous region. Above this region, a region where both microcrystalline and amorphous phases coexist is observed. What follows is a region of a more homogeneous μc-Si:H phase.[24]

Nanocrystalline Si (nc-Si), or more frequently known as microcrystalline Si by other authors/researchers, will be differentiated in this thesis. In light of the already discussed different properties of Si QD and microcrystalline Si, it would be appropriate to distinguish the two materials and call Si QD, which are crystallites of only a few nm in size, nanocrystals or nanocrystalline Si. We will approximate the shape of these nanocrystals as spherical.[25]

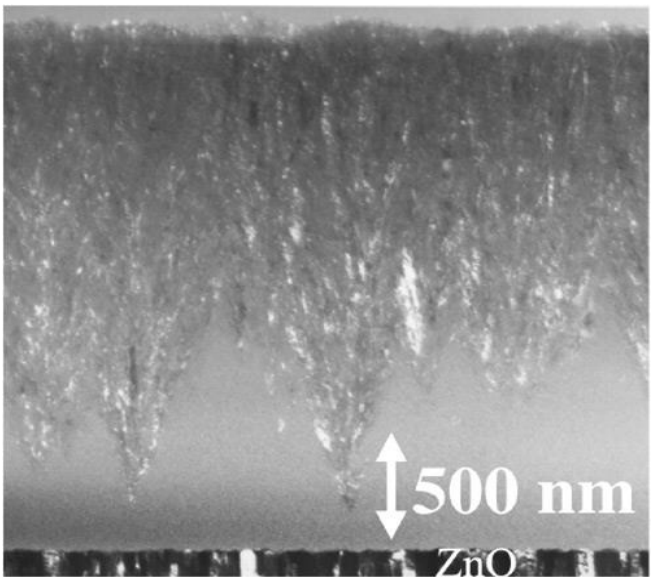

Figure 5) TEM micrograph of hydrogenated amorphous (bottom) and microcrystalline (top) Si layer grown on ZnO substrate.

Si Quantum Dot Solar Cells

A notable material for QD-SC is silicon. QDs of this material would fulfil two major advantages over other materials. Firstly, it is widely available with no shortage of supply of the raw material. Secondly, while current marketed PV cells uses thick Si wafers, Si QDs cells require only thin film that coupled with abundance translates to a lower cost for film production. Another advantage worth mentioning is the non-toxicity of Si.[26] Bulk silicon has an indirect band gap which means it is not easily excited by illumination as the optical transition must be mediated by a phonon that transfers momentum to an electron. This process does not happen readily, so a thick layer is required to compensate.[27] The result is that it shows a weak light absorption. The strong light absorption of Si QDs is an attribute of a direct-optical transition made possible by two effects. One is the already mentioned energy band gap dependency on the QD size, because of quantum confinement. The second is the large surface/volume ratio, where the surface composition is also important in determining the band structure. These can lead to several magnitudes of higher radiative electron-hole recombination rates.[28,29] Si nano-crystals with diameters less than the exciton Bohr radius (4.9 nm for Si) are typically characterized as quantum confined.[30,31] Si QD-SC could allow for instance a design of a solar cell incorporating Si QD-SC in tandem, i.e. a multi-junction cell, for higher efficiencies. Such a tandem cell would consist of two or more stacked cells with the QDs cell(s) with the larger band gap on top and the cell with the smaller band gap on the bottom. Light of longer wave lengths would pass the transparent upper layer and then be absorbed by the bottom layer. This allows for the design of efficient light absorption for every part of the solar spectrum and lead or add to higher efficiency conversion solar cells.[32]

Solar cell technology overview: past to present efficiency improvement

Figure 6 shows a chart with the progress of all different solar cell technologies in research labs with the efficiency on the Y-axis plotted against the year 1975 till 2015.[33] Note the right-hand side of the graph shows the highest efficiency attained so far for each type of material. We see that single crystal Si cells has peaked at its efficiency of 25% in 1999 and has remained so since then. For Thin-Film Technologies

most of the cell types have seen a very modest growth in improving the cells in recent years. This reminds us that the current designs of c-Si and older thin film technologies have for the majority matured and are highly optimised. This leaves few and modest improvements to cell design in the foreseeable future, realistically.

Generally, we see that overtime research increases understanding about conversion loss mechanisms and new way are found to fix them. Another way to improve cell is to concentrate light on the cell by way of light-trapping schemes (concentrator). Multi-junction cells have been at the top of the efficiency chart for some years by integrating and stacking different solar cells, so that each cell absorbs its own part of the solar spectrum to reach the efficiency of 44.4%. Of the new generation solar cell types, some worthy to note are QD cells, organic cells and perovskite cells. The latter has already surpassed the highest efficiency achieved with thin film a-Si:H cells. The projection is that emerging PV cells will continue to improve in efficiency, with older cell technologies benefitting from the increase in knowledge. Another prediction is that new concept solar cells will continue to be introduced.

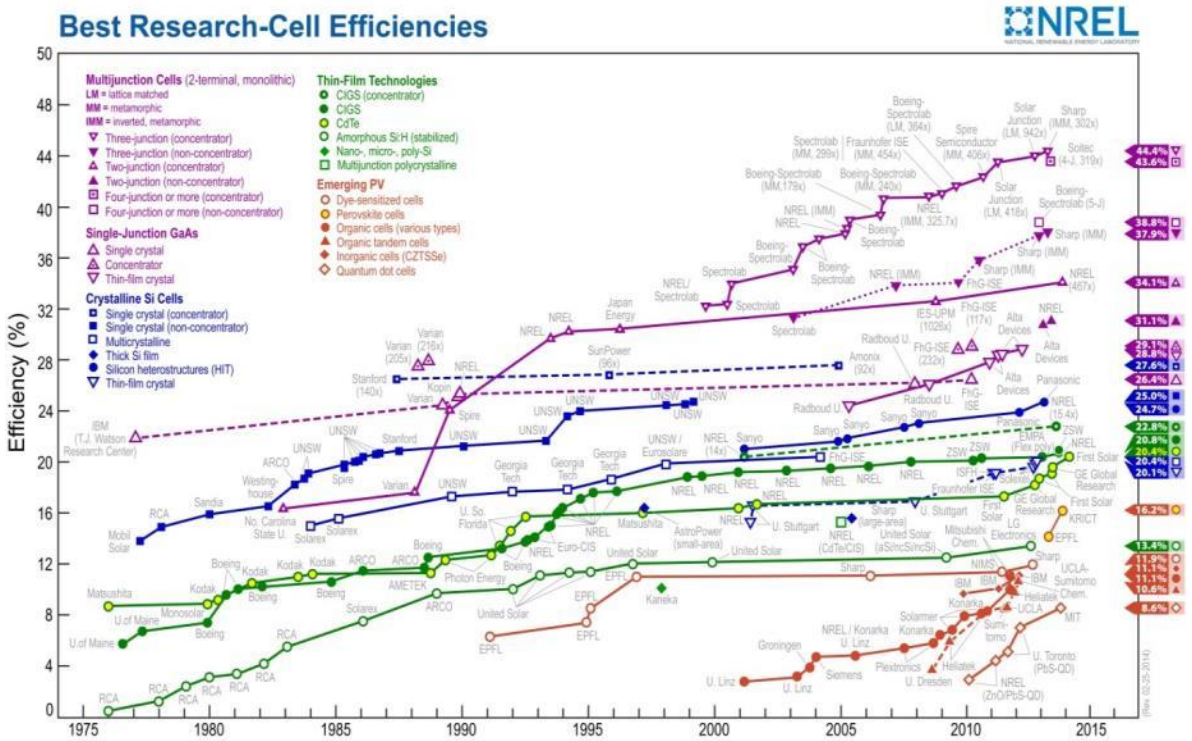

Figure 6) Yearly efficiency progress of the best solar cells made by researchers distinguished for every type of solar cell.

Goal and scope of research.

The goal of this research project was to create Si QDs and make a Schottky Solar cell. For this purpose, several characterisation techniques were used to determine the size, electrical and optical properties of the synthesized Si nanoparticles. A cluster source apparatus was used to create Si QDs and deposited on a substrate. To create particles of the correct size, an optimal set of parameters such as aggregation length, gas flow and RF power was found. The following research question and sub questions were made:

Research Question:

Can we obtain the correctly sized silicon nanoparticles using the nanocluster source, what are their optical, electronic properties and then can we make a Schottky solar cell of the Si QDs?

Sub Questions:

- Which experimental parameters (gas flow, magnetron power, aggregation distance) will yield the correct size of the Si nano particles for use in Schottky solar cell?
- What are the particle size and size distribution of the nano particles determined with AFM & what is the structure determined by TEM?
- What are the optical and electronic properties of the nanoparticles determined with UV-Vis absorption, Raman and luminescence spectroscopy?
- What is the efficiency of the Si QD solar cell and how can we improve it?

Atomic Force microscopy (AFM) was initially used to study the particle size by taking micrographs and subsequent analysis by software. After some trial runs to determine the correct parameters, particle characterisation was performed with Transmission Electron Microscopy (TEM) in University Utrecht and High resolution TEM in TU Delft on successfully made samples. Optical properties of the Si clusters such as luminescence, photo-excitation and decay time were investigated with emission spectroscopy, excitation spectroscopy and time-resolved emission spectroscopy. The crystalline and amorphous Si ratio was determined with Raman Spectroscopy. Further optical absorption measurement was performed with UV-Vis. Finally, an attempt to make Schottky solar cells on Si nanoparticles was made by adding conductive layers and these were tested in a Solar Simulator in Eindhoven for spectral response.

The cluster source apparatus produces nanoparticles by method of magnetron sputtering a Si target (99.999+% pure) in ultra-high vacuum conditions, after which the saturated cloud of atoms condenses in the form of clusters. Argon, which is an inert gas is mixed with the cloud of Si atoms and particles, and transports them through an aggregation tube. The particles then go through an aperture and are deposited on a suitable substrate.[34]

2. Methodology

Theory of Sputtering Operation

Sputtering is a thin film coating technique where energetic particles bombard the surface of a solid and liberate atoms in a low-pressure gas. The solid usually is a disc that (also called the target) is bombarded by ionized gas ions such as an inert gas like Argon, which transfers its momentum to the atoms. The first application of this was seen since the 1940s to make thin film coatings and was called diode sputtering. The basic principle of sputtering is based on the glow discharge, where plasma is generated by applying a voltage between a cathode and an anode in a low pressure gas. A direct current runs (DC) from the cathode (minus) to the anode (plus). At a certain threshold electrons have enough energy to ionize the gas, producing positive ions. These ions accelerate towards the cathode and transfer their momentum to the surface, producing secondary electrons and sputtered atoms. It is noted that the sputtering of the target is a sublimation process and also depends on the surface binding energy of the target atoms. The surface binding energy can be equated to the heat of sublimation, which is the amount of energy that is needed to bring an atom in a solid to the gas phase.[35] The secondary electrons continue to ionize more gas molecules and increase the sputtering rate. The generated plasma has a characteristic glow due to the radiative relaxation of excited electrons that then emit photons of a specific wavelength with respect to the used gas. In a cluster source, the cloud of atoms then travel through the aggregation region where the atoms condense into clusters. After the clusters pass through an aperture, they are deposited on the substrate (see figure 2.1).[36] There are two important conditions for sputtering to work. Firstly, plasma of sufficient energy should be generated from either a DC or RF electrical discharge. Secondly, the freed atoms should be able to reach the substrate material without losing too much energy by collisions with the carrier gas. That is why a vacuum of 10^{-2} mbar or better is needed, so that the mean free path, the average path length between each collision for an atom, is long enough. A mean free path that is too short means the clusters will hit the wall of the aggregation region and be lost through diffusion. This same vacuum condition also works against the sputtering process, because sufficient gas ion collisions at the target surface are needed for a high sputtering rate. The plasma has to be formed a short distance away from the target surface (corresponding to the mean free path of the secondary electrons). On the other hand, a pressure that is too low, will result in electrons ionizing the gas too far away from the surface, or even reach the anode without collisions at all. [37]

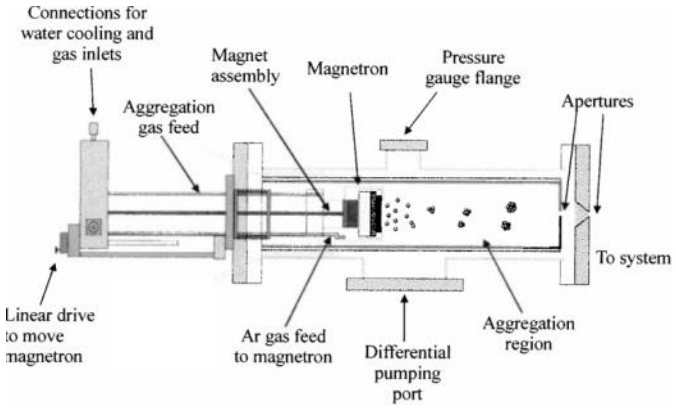

Figure 2.1) Schematic drawing of the NC200U-B nanocluster source. The substrate can be directly placed behind the aperture.

Magnetron sputtering

Given its inefficiency, it took decades for the technique to be improved to a magnetically enhanced version called magnetron sputtering. This involves putting a permanent magnet/pole piece assembly behind the target, which together with the anode and cathode form the magnetron source (see figure 2.2a & 2.2a).[38] The pole piece is a material such as soft iron that serves as an extension of the permanent magnet to confine magnetic fields to a smaller area. Magnetron sputtering has advantages over other thin film coating techniques such as thermal evaporation and electron-beam, such as a fast deposition rate, uniformity of film, automation for large-scale processes and the ability to sputter different kinds of materials. The magnetic field is arranged as such that a magnetic field sticks partly out of surface and traps electrons that move in to these so called 'race-tracks'. This leads to significantly increased plasma production and thus more sputtering. A lower operating voltage is another benefit, as the impedance of the plasma, the difficulty for a current to flow in the plasma, is lower and so the required voltage drops from several kV to several hundred V. A feature of the tunnel-shaped magnetic field that penetrates the surface is that sputtering overtime will give a distinctive wide groove to the target (see figure 2.3a-b). That also means about only roughly 20% of the target will eventually be utilised and the rest is discarded. About 80% of power is converted into heat that is dumped mostly into the cathode, so the useful power going into sputtering atoms is about 20%. To prevent the cathode from overheating, it must be water-cooled and that is the reason it is often made out of copper to conduct heat and electricity.[39]

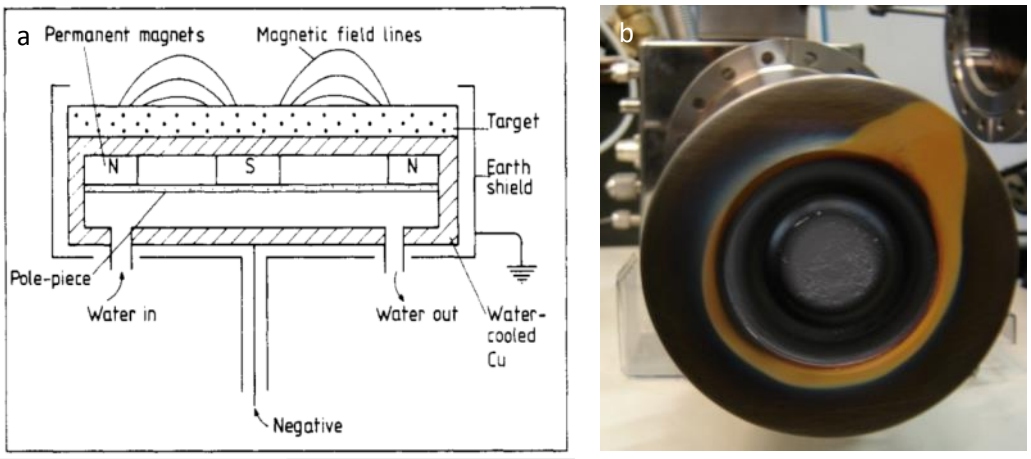

Figure 2.2a) Cross-section of a magnetron source scheme (simplified). (b) Front-side view of magnetron source with Si target. Nanoclusters of deposited Si are seen on the earth shield (light

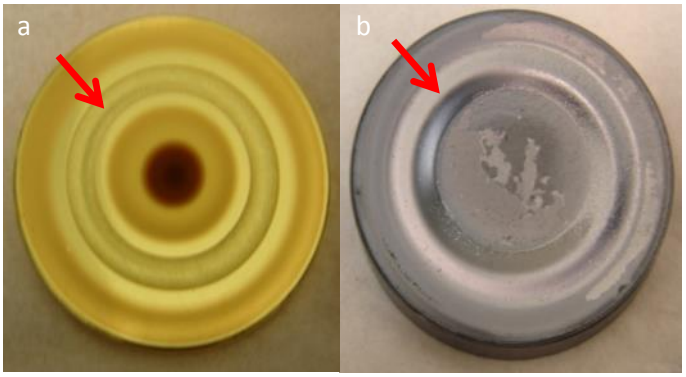

Figure 2.3a) Gold and Silicon (b) targets that have been sputtered. Note the distinct circular erosion profile (red arrow).

RF magnetron sputtering

A NC200U-B cluster source (figure 2.4) was used to produce Si nano-clusters with RF (radiofrequency) magnetron sputtering. This section will explain what the technique differs from above. Unlike DC sputtering which is used for conducting materials such as metals, RF sputtering is required for sputtering materials which do not conduct electricity, i.e. are electrical insulators and semiconductors like Si. This necessitates the use of more specialized equipment. An RF generator is needed that applies alternating current (AC) with a typical frequency of 13.56 Mhz, to create a so-called DC sheath potential on the surface of Si target by capacitively coupling. The origin of this DC potential comes from the fact that electrons are much lighter than the positive ions, and hence has a higher mobility in a constantly changing electrical field. Consequently, both positive ions and electrons in a plasma move in opposite directions in the field and different distances for each half cycle, which means that there a difference in ion and electron current. Since the capacitor is capacitively coupled to the surface, no net charge transfer is possible. The cathode surface becomes negatively biased (the electrons are screened by a sheath of positive atoms), and so a DC negative voltage is produced that allows sputtering. In addition to this, an impedance matching network must also be used in combination to deliver the maximum power output to the plasma. This is done to avoid power losses and potential equipment damage. An AMR150R, automatic impedance matching network was used that automatically adjusts the impedance of the load to the impedance of the RF generator, which was a model RFG 600 13-27 MHz. The impedance describes the resistance for an AC current, similar to the measure of resistance in a DC circuit, but more complex due to the change in electric current direction, and it includes the inductive and capacitive reactance. The inductive reactance is proportional to the amount of change in the current and also the AC frequency, which produces an opposing electromagnetic force that reduces current flow (induction). The sputtering yield is the percentage of sputtered atoms for every positive ion that bombards the surface. A disadvantage of RF magnetron sputtering is that it generally has a lower sputtering yield (~10% that of DC magnetron sputtering), because the materials used are not as heat conductive and shock resistant as metals. Therefore, the power that is typically used is lower to prevent overheating and damage of the target.[40]

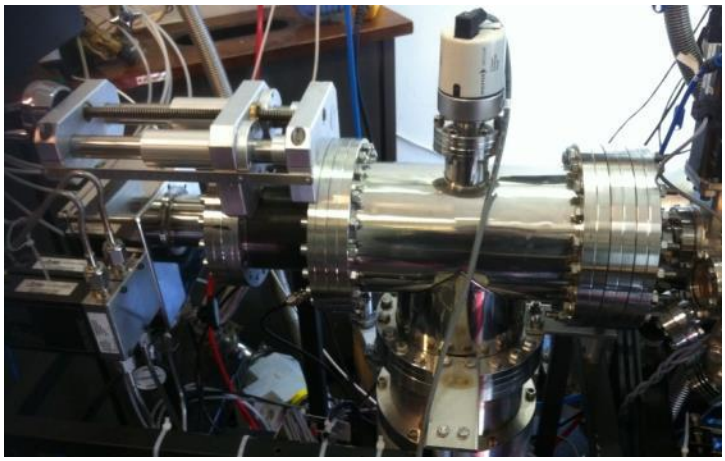

Figure 2.4) The NC200U-B cluster source depicted here was used to create the nano-clusters. The central/deposition chamber on the right edge (a small portion of it is shown) contains the substrate.

Sample preparation, cleaning & loading

Different substrates were used for sputtering Si clusters. These were glass, Si wafers and 80nm thick ITO (indium tin oxide) on glass that were cut in approximately 1 cm by 1 cm sizes. Contamination (dust in particular) of substrate surface must be removed by cleaning. For glass and ITO on glass substrates, these were put in iso-propanol and placed in a sonication bath for 2 minutes to remove contaminants off the surface. They were then placed on KIMTECH SCIENCE Precision wipe tissues and gently dried. The remainder of i-propanol on the substrates evaporated quickly at room temperature. This was followed by placing the substrates in a sample holder and compressed air was used in short bursts to remove any remaining dust. For Si wafers, the sonicating in iso-propanol step is not necessary. Finally, the sample-holders were loaded in the load chamber (see figure 2.5), where they can be transferred to a central chamber. The central chamber is where the Si clusters are deposited on the substrates. Failure to remove any remaining dust contaminants in the case of ITO would short-circuit a solar cell. Dust particles could also interfere with the AFM and TEM imaging techniques.

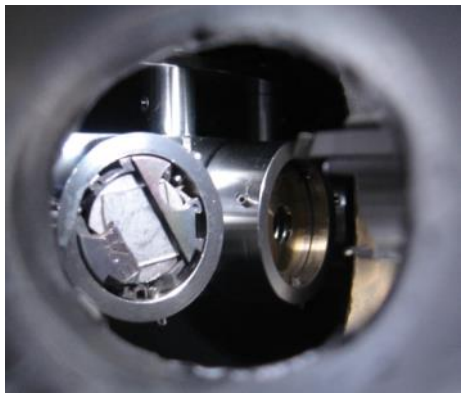

Figure 2.5) The inside of a load chamber where a rectangular-shaped glass sample is held in place by a coin-sized sample-holder inserted in a slot of the carousel. To the right of this slot is an empty slot with no sample-holder.

Cluster source parameters

Three parameters of the cluster source can be varied accordingly to obtain the desired particle size, which are the carrier Ar/He gas flow, RF power and the aggregation length. The aggregation length can be varied from 20 to 80 mm by manually moving the magnetron source towards the aperture. A long aggregation length means that particles travel further and stay longer in the aggregation tube. The result is large clusters. On the other hand, a shorter aggregation length results in the deposition of smaller clusters on the substrate. A higher gas flow of Ar increases the pressure, thus reduces the free mean path of the clusters. This means more collisions and larger clusters, but also more clusters are lost due to diffusion to the walls. Increasing the RF power transfers more power to the plasma and so should give a higher sputtering rate, due to a higher ion bombardment rate. This then should give larger clusters. However, figure 2.6 shows that the cluster size indeed increases with increased power, but at 60 watts it levels out and even drops for a high Ar gas flow of 18 and 26 sccm.[41] Unfortunately, it turns out that some combinations of these parameters can give unexpected results (larger or smaller particles), which shows the relationship of the parameters needs to be better understood.[42]

The helium that was used in the cluster source contributes little to the sputtering rate compared to argon, because the ions have lower mass and therefore insufficient momentum to sputter effectively. The purpose of helium was to stimulate the aggregation to smaller particles due to thermodynamic considerations. It also contained a fraction of hydrogen (10% volume fraction hydrogen) to enhance sputtering. Hydrogen ions are lighter than helium and carry even less momentum than helium, but nonetheless increase the sputtering yield through another mechanism. Hydrogen ions can chemically bind to the target surface and enhance the evaporation of surface bound target atoms into the plasma. This effect is further improved by the magnetic field. Once evaporated into the plasma, the hydrogenated target species can dissociate due to the electrical discharge, or from the UV light of the plasma or when it is heated through collision with the surface substrate.[43]

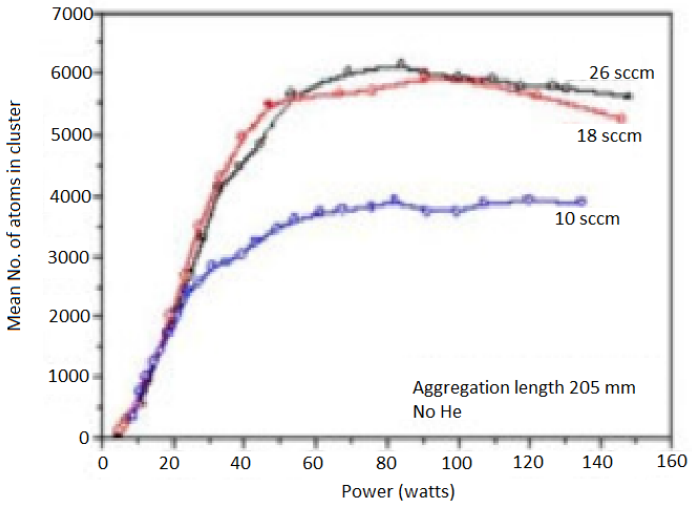

Figure 2.6) Atoms in cluster versus magnetron power and 3 different Ar gas flows at one aggregation length. (Picture enhanced for clarity)

Turbo pump, background/operating pressures

Turbo pumps were used to reach ultra-high vacuum (UHV) in the cluster source, central and load chamber (figure 2.7a). The central and load chamber also had their secondary pump, both of which are VACUUBRAND diaphragm pumps model MD 4 VARIO-SP with a pumping speed of 3.3 m^3/h (see figure 2.7b). The cluster source uses a different secondary pump that was a Pfeiffer rotary vane vacuum pump powered by an AEG motor and a pumping speed of 82 m^3/h depicted in figure 2.7c. Besides the need for a high mean free path of the sputtered atoms, the UHV environment contains very little undesired reactive gasses such as oxygen and contaminants like dust. The normal background pressure of the deposition chamber and the cluster source chamber was 1.3-1.5E-5 mbar and from 5.0E-9 to 8.0E-8 mbar, respectively. The higher pressure in the deposition chamber was attributed to a leak. In practice, this proved not to be much of a problem for sputtering. The background pressure was slightly above 5.0E-9 mbar, but after Si deposition and subsequent oxidation of the Si on the inside of the aggregation tube, the pressure dropped below 5.0E-9 mbar, which was outside the measurement range of the vacuum gauge. The operating pressure was noted as 1.3-1.5E-4 mbar and 1.7-1.9E-3 mbar for the deposition and cluster source chamber, respectively. The pressure difference between these two chambers at operating pressures allows the gas and clusters to diffuse to the deposition chamber from the cluster source.

Figure 2.7a) Turbo pump of the Nanocluster source. (b) Diaphragm pumps of load and central chamber. (c) Rotary vane vacuum pump with motor.

Luminescence equipment

Measurements of photoluminescence (PL) were done by recording emission and excitation spectra on an Edinburgh FLS920 dedicated fluorescence spectrometer with a single monochromator, a Hamamatsu R298 detector and a Xe900 continuous Xenon Arc lamp as excitation source (figure 2.8a, set-up 2). Emission spectra measurements were carried out at an excitation wavelength of 375nm. PL lifetime measurements were done on another Edinburgh FLS920 equipped with a Hamamatsu H4722-02 photo sensor module, double monochromator and an Edinburgh 375 EPLED nm picosecond pulsed diode laser as excitation source (figure 2.8b, set-up 1). The sample holder presented in figure 2.8c was used in all measurements. Both set-ups have the incident beam (Laser source or Xe lamp) at a 45 degree angle to the sample surface, while the detector detects photons emitted from the surface travelling in a direction orthogonal to the incident beam direction.

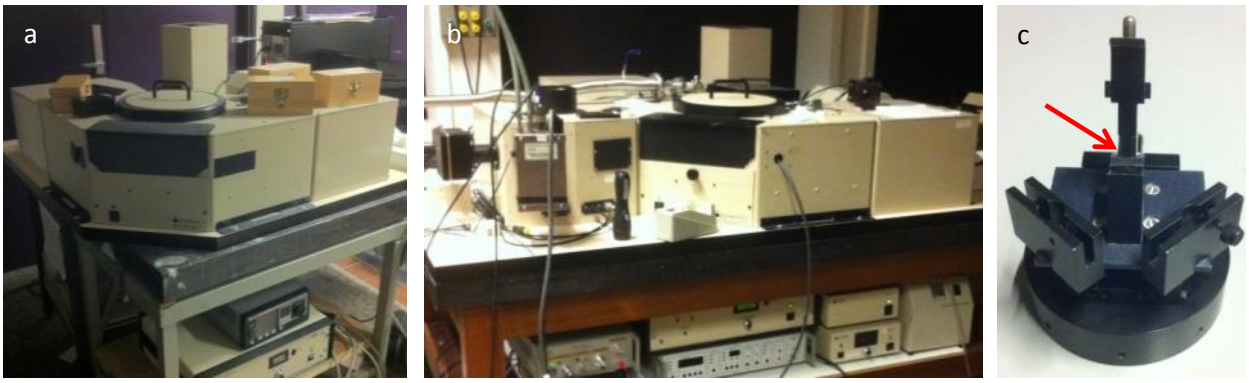

Figure 2.8a) Edinburgh FLS920 (Set-up2). (b) Edinburgh FLS920 (Set-up 1). Laser module is not shown. (c) Sample holder. Red arrow points to where sample is supposed to be placed.

Raman Theory & Instrumentation

Raman spectroscopy works on the principle of non-elastic scattering of monochromatic photons of an excitation source, by a material such as a crystal. Photons propagate through space as electromagnetic waves that interact with the electron orbits of a bond in a solid for example. The electrons in a cloud are disturbed by the passing of an external electrical field and start to oscillate, which changes the local electron density in an electron cloud. This causes a periodic charge separation that is called an induced dipole moment. When the electrons relax, they emit photons in different directions (scattering). The majority of the photons that are emitted are of the same wavelength as that of the incidence photons and so are elastically scattered. A tiny fraction of photons are in elastically scattered (Raman scattering) by energy transfer from a photon to a vibration of a molecular bond, resulting in photons with a longer wavelength called Stoke's shift. The energy transfer can also happen vice versa, which then it is called Anti-Stoke's shift and emitted photons have a shorter wavelength. Generally speaking however, the chance of Stoke's Shift happening is much higher than Anti-Stoke's shift. A laser is commonly used as the excitation source as it can be focused on and study small sections of the sample.[44]

Raman spectra were recorded with a Renishaw InVia Raman microscope (figure 2.9) using an Ar-ion Spectra-Physics laser (Model number: 163-M42-010) as the excitation source which excites at 514nm. [45] The signal intensity versus the Raman shift expressed in wavenumbers (cm^{-1}) is measured in a Raman spectrum. The excitation wavelength is chosen taking in account the extent of the Raman shift,[46]

Figure 2.9) Renishaw Invia Raman microscope that was used.

Raman spectra allow the determination of the crystalline fraction, known as X_c and is found by the following equation:

$$X_c = (I_{520-x} + I_{520})/(I_{480} + I_{520-x} + I_{520})$$

$I_{520\text{-}x}$, I_{520} are the integrated intensity of the µc-Si and the c-Si which when both are added up to be the crystalline fraction of the sample. µc-Si displays more red-shift (Raman shift of x cm^{-1}) and peak broadening as the crystallite size gets larger. I_{480} is the integrated intensity of a-Si. 480 and 520 cm^{-1} refers to the Raman shift of the a-Si and c-Si peak, respectively.[47]

Dektak

A Veeco Dektak 8 surface profilometer seen in figure 2.10 was used to determine the thickness of a select few samples.[48] A sharp tip measures the height profile by dragging it along the surface applying a very weak force. A horizontal cut in the Si layer was made with a small knife. This exposes lowest point of the Si layer, so that when a tip scans over this cut that would then allow the determination the average height difference between the top and bottom of the film, which also equals the thickness.

Figure 2.10) Veeco Dektak 8 surface profiler

UV/Vis absorption theory & equipment

UV-Vis is an optical technique that relies on the light absorption of photons typically in the ultraviolet and visible region (but also in the near infrared) by a solid or liquid. Absorption of light by molecules cause transitions to higher energy states which give rise to broad bands as transitions with different energies are possible. The molecules subsequently lose energy through non-radiative relaxation. The optical technique involves sending light through, for example a solid sample held in position, where the incident light (I_0) to the sample is compared to the transmitted light (I) behind the sample. Transmittance, T, is defined as (ranging from 0 to 1):

$$T = I/I_0$$

The absorbance, A, can also be defined in terms of transmittance:

$$A = -\log T$$

The law of Lambert-Beer is given by:[49]

$$T = e^{-\propto l}$$

α = absorption coefficient of material usually given in cm^{-1}

l = optical path length through material (or thickness for a film) given in cm

The law states that the light absorption of a material is proportional to the number of light absorbing molecules or atoms leading to the relation between transmittance, and the absorption coefficient and optical path length. The absorption coefficient depends on the material and the conditions of the measurement such as the wavelength, temperature and spectrometer.[50]

UV-Vis measurements were done on a Vertex 70 FT-IR spectrometer (Figure 2.11). A reference absorbance spectrum was recorded of glass prior to the sample measurements. The software corrects the recorded spectrum of the sample by subtracting the absorbance of the reference spectrum.

Figure 2.11) Vertex 70 UV-Vis spectrometer.

The absorption coefficient can be expressed as a function of the absorbance, A, and thickness, t[51]:

$$\alpha = \frac{2.303A}{t}$$

A Tauc plot can be constructed to yield the energy band gap of an semiconductor with an indirect or direct band gap. On the y-axis of the Tauc plot, $(\alpha h\nu)^n$ is plotted against $h\nu$ on the x-axis. *h* is the Plank constant ($4.14*10^{-15}$ eV/s), *v* (s^{-1}) is the light frequency given by the formula v = c / λ and *n* depends on if the film has an indirect or direct band gap. *c* is the speed of light constant ($3*10^8$ m/s), λ is the wavelength of light (m).[52] The linear part of the plot that begins from the lowest energy (eV) is fitted with the Origin 8 program. The $h\nu$ value for when the linear fit intersects with the x-axis (y = 0) gives the value of the energy band gap (eV).[53]

Atomic Force microscopy (AFM) theory & equipment

Unlike conventional microscope techniques like a light microscope and TEM, AFM does not involve the focusing of photons or electrons in a narrow beam on a sample, nor does it image a 2-dimensional image. Instead, the technique involves scanning a sharp tip (called the probe) very close over the surface

of a material such a semiconductor, in a raster like pattern. While the probe scans the surface line by line, the force between the interaction of the probe and surface atoms is measured and kept constant. The probe 3-dimensional movement is tracked, so that an image of the surface topography can be compiled (figure 2.12). [54]

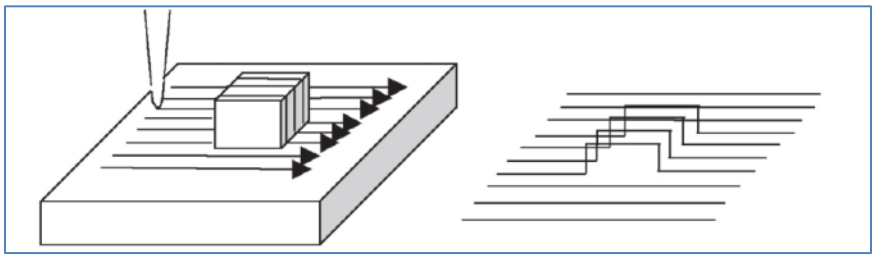

Figure 2.12) A tip scans the surface (left) and builds up the generated image (right) line by line.

This allows the accurate height determination of surface features on the nm scale. The probe is attached to a cantilever (which acts like a spring) and is lowered towards the surface, such that the weak Van der Waals interaction causes an attractive force between the probe and surface. As a result the cantilever bends towards the surface. At a certain lower point the probe-surface interaction turns into a repulsive one and the cantilever bends away from the surface (see figure 2.13). The van der Waals interaction is a sum of relatively weak, short-range attractive and repulsive interaction force between atoms. Hooke's Law is used to determine the interaction force given by:

$$F = -k * x$$

F = force acting opposite and equally to the force that bends the cantilever (N)

k = spring constant (N/m)

x = cantilever deflection (m)

The cantilever bends when its spring constant (~0.1-1 N/m) is lower than that of the surface. The amount of deflection is dependent on several factors such as the used tip, the surface and the stiffness of the cantilever. The tip is usually composed of Si_3N_4 or Si. The spring constant can be changed by varying the material or length of the cantilever. [55]

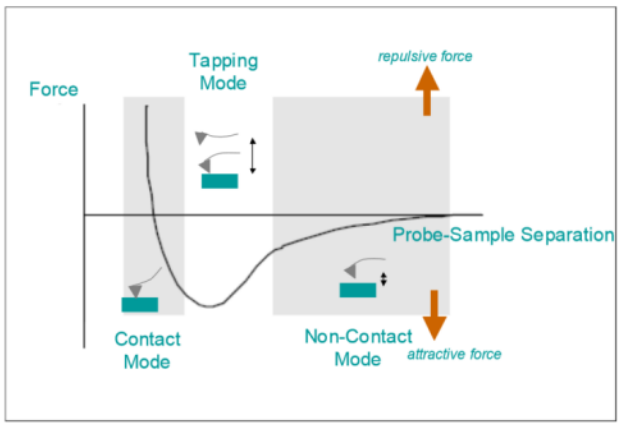

Figure 2.13 The repulsive (positive) and attractive (negative) force of the probe-sample plotted against the probe-sample distance. Three different AFM modes exist depending on the region.

Three different AFM modes are each characterized by a different probe-sample distance (see figure 2.13 again). When the probe is close to the surface while scanning, it is repulsed (<0.5nm). This is referred to as contact mode. The deflection of the probe by the surface is held constant by a feedback controller,[56] which is done by continuously adjusting the height with a z-motion generator (figure 2.14). The deflection is proportional to the force the probe experiences, so a force sensor is used to measure the force that then outputs a voltage signal to the feedback control. The AFM block diagram in figure 2.14 also shows how the feedback controller sends out height information of the probe. The X-Y motion generator is responsible for the lateral scanning motion of the probe and so the obtained X-Y and Z coordinates are combined to generate an image of the surface topography. Both the Z- and X-Y motion generators use a piezoelectric material that is capable of making precise movements on the angstrom scale, such as amorphous $PdBaTiO_3$. Piezoelectric materials contract or expand depending on the voltage applied, and also show the reverse effect when mechanical force is exerted on the material. A common expansion coefficient is ~0.1 nm/volt depending on material and shape.[57]

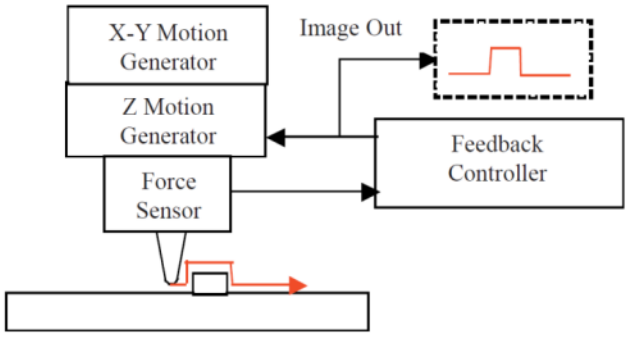

Figure 2.14) AFM block diagram

Tapping mode is another AFM mode that is a softer technique. The cantilever is oscillated at its resonant frequency while scanning at a further probe-surface distance (0.5-2nm). The resonance frequency is a

natural oscillating frequency associated with an object when a force is exerted on it. The probe only has regular contact with the surface each time the cantilever oscillation is at its lowest point. A constant oscillation amplitude (20-100nm) ensures that the probe-surface forces are also constant. Compared to contact mode, tapping mode has a slower scan speed, but better image resolution of surfaces that would otherwise be damaged or disrupted. The AFM micrographs in this thesis were all taken with tapping mode AFM.

The third AFM mode is non-contact mode and it is similar to tapping mode in that it also has an oscillating cantilever, but it relies on the attractive van der Waals forces that are further away from the surface. The feedback loop checks for any changes these forces cause in the oscillation amplitude. Of all modes, non-contact mode generates the lowest force on the sample surface, but suffers from a poor resolution due to contamination of the surface in a normal measuring environment. This is solved by operating in an UHV. [58]

A light lever is typically used as a force sensor (figure 2.15a) for AFM (LL-AFM). A laser beam is reflected off the cantilever to a photo detector. The photo detector is sensitive to any changes to the reflected laser path that are caused by the cantilever deflection, as that will slightly change the position of the laser spot on the detector. A disadvantage of this is that every time the probe is switched, the laser needs to be re-aligned again such, that the laser spot strikes the photo detector and a sufficient output signal is read.[59]

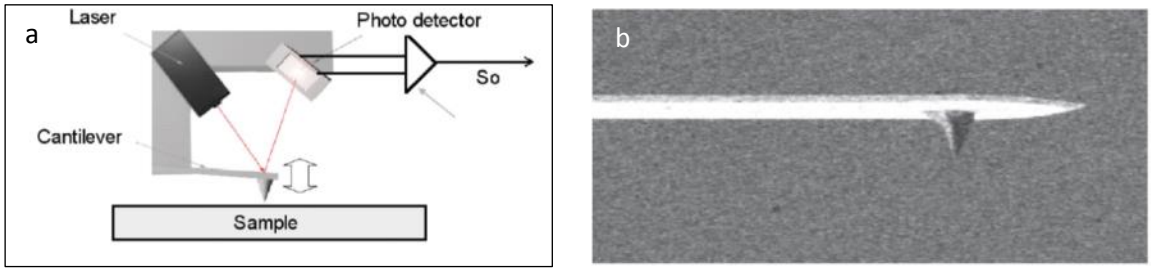

Figure 2.15a) Light lever force sensor and (b) the cantilever with probe pointing downwards.

Although AFM has good vertical resolution, the lateral resolution suffers from an effect called tip-convolution, which is present in all AFM images. This effect is more pronounced when the probe tip is dull or has a big radial curvature (low aspect tip, figure 2.16). Generally, this effect is not noticeable when the probe is small compared to the surface features, but it becomes more critical with small nm-sized features that lead to broadened features. It is this reason that makes size determination of small nano-particle on surfaces unreliable when the lateral dimensions are taken instead of the height. The probes used in practice are not ideally sharp (~10nm at the end) and hence an approximation of the surface topography is imaged.[60]

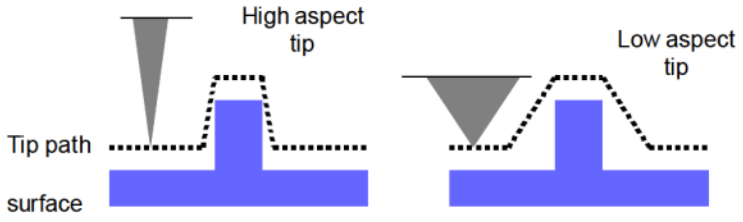

Figure 2.16) A scan line over a feature with a sharp tip (left) and the same scan line with a dull tip (right). Tip convolution is the reason why the dull tip does not scan the surface feature properly.

AFM was used, because it allows relatively fast nm-resolution image capture of surfaces with little to no sample preparation. A MultiMode Scanning Probe Microscope with a Digital Instruments Nanoscope IIIa SPM controller was used (figure 2.17a & 2.17b). Bruker OTESPA AFM probes (figure 2.18) for tapping mode operation were used. The microscope is on a slab that was lifted mid-air by four rope springs to reduce background noise during measurements.

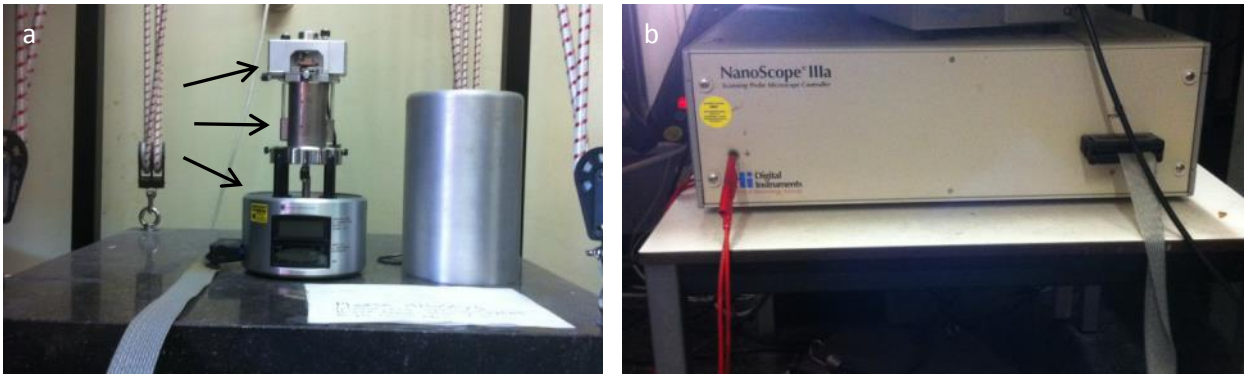

Figure 2.17a) MultiMode AFM microscope. From bottom to top (black arrows): Base, scanner and optical head. The noise isolating cylinder-shaped metal cap next to the microscope is placed over the optical head. (b) Nanoscope IIIa SPM Controller

Figure 2.18) Bruker AFM tips

TEM

Transmission Electron Microscopy (TEM) is an important technique to visually study the structure of the samples that are nm-sized. It involves an electromagnetic lens focusing of an electron beam on a thin substrate containing the sample of interest, where a part of the electrons are absorbed by the atoms and molecules, depending on the thickness and type of material. A portion of the original beam is transmitted. The transmitted beam falls on a detector plate that then translates it into a white-grey micrograph. Different TEM set-ups are available, with electron beams with higher energies (kV) offering more resolution, but at a more expensive price and risk of destroying the sample. A FEI Tecnai 10 (figure 2.23) with a standard TWIN objective lens and a SIS CCD camera Megaview II was used for imaging. The electron source is a W emitter with a voltage range of 20-100 kV. The machine offers a point resolution of 0.34 nm.[61] A Tecnai 12 was also used with a voltage of 120 kV to capture micrographs.

A FEI Titan 80-300kV, which utilizes the High-Resolution Transmission Electron Microscopy (HRTEM) technique (figure 2.24) was also used to study the clusters in more detail. It offers more details at higher magnification due to the higher energy electron beam and resolution (point resolution 0.09 nm).[62]

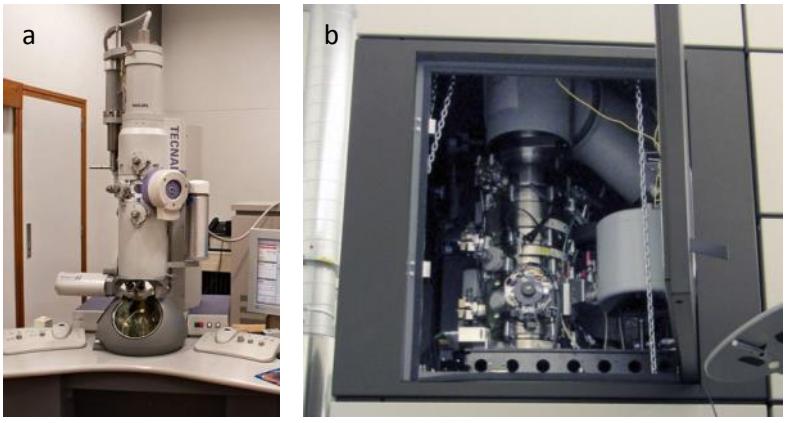

Figure 2.19a) FEI Tecnai 10 (b) FEI Titan HRTEM

Silver evaporation on Si layer

After the right Si layer was made on top of the ITO, Ag contacts were prepared through a custom thermal vacuum evaporation unit used to condense an Ag layer on the Si layer. A simplified scheme of the unit is depicted in figure 2.20a. A few grams of 99.99% pure silver was cut in pieces and placed in the tungsten crucible. The crucible was resistively heated to a high temperature by applying a current of 5 A, until all the silver in the crucible was evaporated. The silver vapour travels upwards in the vacuum, where it is only allowed pass through the holes of a mask (example shown in figure 2.20b) where it condenses on the silicon layer. Each hole has a diameter of 2mm, so that each sample has multiple silver contacts and thus effectively creating multiple individual solar cells. A turbo pump creates a vacuum environment, which reduces the boiling point of Ag, removes reactive gasses like oxygen and increases the mean free path of silver vapour. The background pressure was lower than 9.9E-7 bar and the operating pressure was ~2.5E-5 bar.

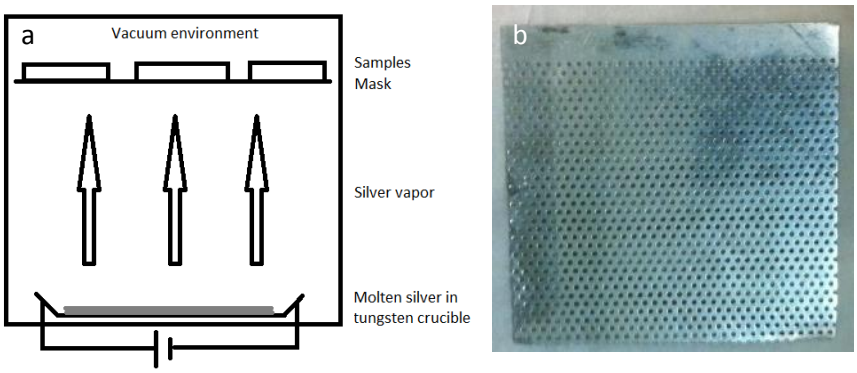

Figure 2.20a) Simplified schematic of the silver evaporation unit. (b) Silver vapour passes through holes of mask and condenses on the substrate. A different metal mask than the one shown here was used.

Multi-meter measurement & silver paint

To avoid the risk of the electrodes damaging the thin silver layer and short-circuiting the solar cell, SPI high purity silver paint was applied for each cell with a thin copper wire attached to the paint and extending outwards. The paint was let to stand at room temperature and dry for at least 2 hours, so that the binder material evaporates and the copper wire is bonded to the paint. Then the whole sample was turned upside down (glass side up) and put on a rectangular glass piece shown in figure 2.21, so light shone directly on the active silicon layer. Then, two copper wires each held by an alligator clip made electrical contact with the copper wire attached to one cell and the other electrode with the ITO.

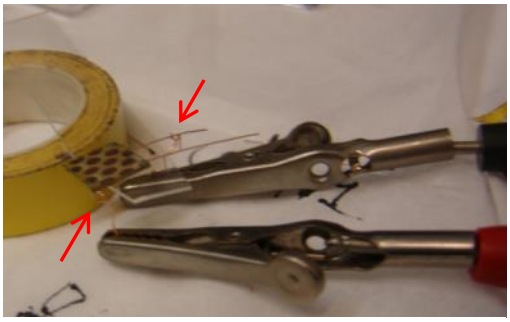

Figure 2.21) Two electrodes measuring the light response from Schottky solar cell. Note that the copper wires held by the alligator clips extend vertically up (red arrows).

Solar simulator

I-V curves were measured in a solar simulator that simulated AM 1.5 G conditions. The model number is WXS-300S-50 made by WACOM and the model with sample is shown in figure 2.28a-b.

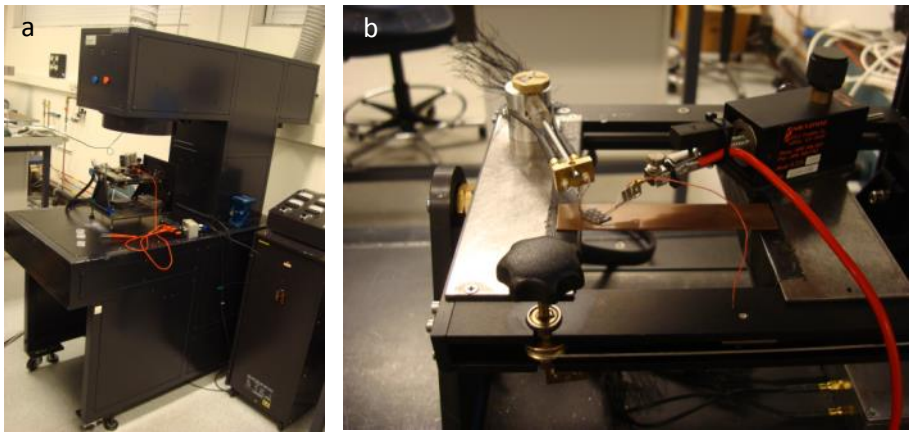

Figure 2.22a) WACOM solar simulator. (b) Electrodes mounted on the sample with no silver paint applied.

3. Results & Discussion

Optimal cluster source parameters

A series of 6 test runs with different cluster source parameters were done to deposit Si on Si wafer substrates to create the samples (CS336-341) seen in the second and third column of table 3.1. RF power and the He/Ar gas flow were varied, while the aggregation length and deposition time was kept constant at 40mm and 2 minutes, respectively. Note that passivation of the dangling bonds at the surface for the Si clusters by hydrogen-termination is likely only a small fraction, because a dilute amount of hydrogen was used for sputtering. After the samples are taken out and exposed to air, the surface is slowly oxidised. Because the cluster source produces an inhomogeneous beam of clusters, the sample is continuously moved in the beam to obtain a homogeneous layer. The cluster source is sputtered for at least 30 seconds, so that a steady stream of clusters and gas is produced before every deposition.

Sample number	RF power (W)	He/ Ar flow (sccm)	Sampling Size (1-10nm)	*Mean size* (nm)	σ (nm)	Cluster Density (10^8 /cm^2)
CS336	40	5/15	55	4.6	2.08	7
CS337	40	10/15	25	~7.6	~1.90	~4
CS338	80	5/15	102	6.8	1.32	27
CS339	80	10/15	69	5.0	1.29	27
CS340	120	5/15	70	4.9	1.41	22
CS341	120	10/15	68	3.5	1.24	19

Table 3.1) Used parameters for samples CS336-341 (2nd and 3rd column). Aggregation length and deposition time were kept constant. Number of clusters measured between 1 and 10 nm diameter size (4th column). Mean cluster size μ, standard deviation σ and cluster density (last three columns).

All samples were studied through height profile images taken with AFM tapping mode of which shown in figure 3.2a is from CS341 and 3.2b is from CS338. It shows that CS341 has a few large clusters seen as the white large spheres that are bigger than 24.2 nm, which are formed by the collisions and aggregation of smaller clusters in the aggregation chamber or coalescence on the surface. Their sizes lie outside quantum confinement range and are therefore undesirable for the solar cell. Statistical cluster size and surface density analysis on all samples was performed with WSxM 5.0 software. The height of +50 clusters, which is the same as the diameter, was determined with the profile function for all samples. The resulting histogram for CS341 is shown in figure 3.3. The other five histograms (CS336-340) are included in appendix A. Note that larger clusters are few in number and are left out of these histograms for clarity. They are left out of the statistical analysis, because the interest is in clusters with

a size range that is close or in the quantum confinement range (1-10nm diameter in size). The calculated mean cluster size, standard deviation (σ) and cluster density are presented in table 3.1.

CS336 and C337 proved to be less interesting due to their wide cluster size distribution and low cluster density. The low cluster density is attributed to the low RF power (40W) that was used, which causes a low sputter yield. The doubling of the He flow seemed to further decrease the sputtering yield and increase the mean cluster size, which means less clusters are in the quantum confinement region. Note however that the calculated values for CS337 are not statistically significant enough to represent the sample, as only 25 clusters were considered from the required minimum of 50. These values can only serve as an approximation.

Using a RF power of 80W or 120W for CS338-341 dramatically raised the sputtering yield, which is expressed by the high surface cluster density. It also follows that the cluster density is not linearly related to the RF power, because a lower density was obtained for 120 W. Two effects were observed with the doubling of the He flow. Firstly, the mean cluster size decreased for CS339 and 341. An explanation for this is that during collisions of the clusters with He atoms, less energy is transferred, leading to less aggregation, i.e. smaller particles. Perhaps during the aggregation of clusters in the aggregation tube, a small fraction of the hydrogen is at any moment bonded to the clusters. More bonded hydrogen increases the energy barrier for cluster growth as not every Si cluster collision results in fused particles (less dangling bonds) and thus limits the growth to some degree. Thirdly, the size distribution is lower which is seen for all samples. The lowest mean cluster size was for CS341 that also has the lowest size distribution and a high cluster density. This is the optimal setting for depositing the most Si clusters that are quantum confined.

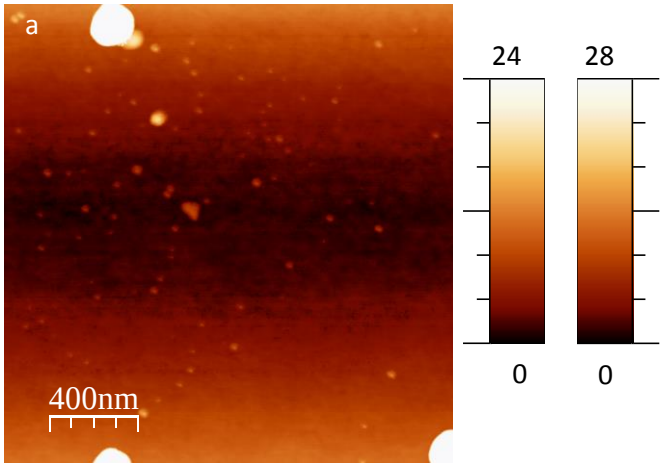

Figure 3.2a) AFM micrograph of CS341 (b) AFM image of CS338. Height scale bar next to micrograph are in nm. Scale size is 2 x 2 µm

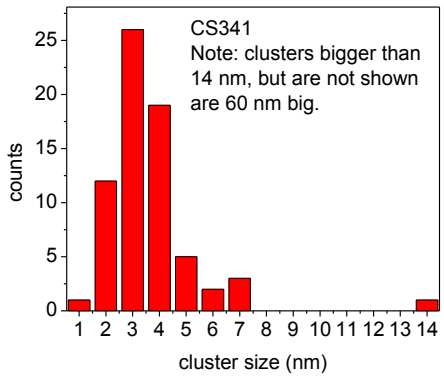

Figure 3.3) Histogram for sample CS341. Larger clusters (+14nm) were not shown for clarity. See appendix for histograms of CS336-340.

AFM (Atomic Force Microscopy)

It is of interest to make sufficiently thick films to characterise them and eventually use these films in a QDSC. To this end, a 30 minute deposition was done using the previously mentioned optimal setting and this was done on glass for optical characterisation purposes. The cluster size was investigated with AFM. The resulting micrographs are shown in figure 3.4a-b, which shows that the Si clusters have formed undesired large clusters (20, 40, 60, … nm) and that they are out of the quantum confinement range. This means that the small clusters first observed on the Si wafer of sample CS341 with AFM favour aggregation to large clusters when longer depositions are used. Several factors play a role in this aggregation. An alternative explanation is that incoming clusters can be deposited on the surface and collide with the clusters already on the surface, which in the case if it has enough energy, coalesces into a larger spherical cluster. This process is proportional to the surface coverage, i.e. the higher the surface cluster density, the higher the coverage and chance of coalescing. Another mechanism of particle growth is coalescing of the clusters which involve surface diffusion. Depending on the type of substrate and surface roughness, small clusters are mobile on the surface and can diffuse over it until they encounter a surface defect or another cluster, so that it may result in coalescing or sticking. This is proportional to the surface coverage. That explains the observation of small clusters with a small diameter at a low surface coverage.

Note that figure 3.4b also shows some white lines that are artifacts due to the probe not scanning the surface correctly by momentarily losing probe-surface contact. The exact morphology of these large clusters will be further explored with TEM in another section.

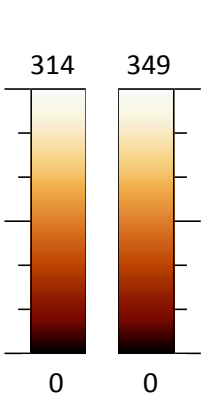

Figure 3.4a) AFM micrograph of CS345 3 x 3 µm scale. (b) Scale size is 5 x 5 µm. Height scale bar is in nm.

Varying aggregation length & selection of 3 samples

One set of cluster source parameters that can deposit small Si clusters of around 3 nm was found (CS341) amongst different settings. We have found that the small clusters form large clusters for long depositions. It was decided to study the effect of varying one parameter setting to study the change in structural, electrical and optical properties. The aggregation length was chosen as the parameter that was to be varied. Depositions on glass were done for 5 minutes (CS425) using the parameters of CS341. Then, the same depositions were repeated twice, but the aggregation length of 20mm (CS430) and 60mm (CS427) were used instead of 40mm (CS425). See table 3.3 for the parameters.

Sample number	Aggregation length (mm)	RF power (W)	Ar/He flow (sccm)
CS425	**40**	120	15/10
CS427	**60**	120	15/10
CS430	**20**	120	15/10

Table 3.3) Sample CS425, 427 and 430 with used parameters for the cluster source.

AFM micrographs were taken of the samples with 20, 40 and 60mm aggregation length. Figure 3.5 shows one micrograph of the sample with 20mm aggregation length. The clusters have coalesced similarly to figure 3.4a-b to large clusters of 50 to 100nm. This was also observed for an aggregation length of 40 and 60mm.

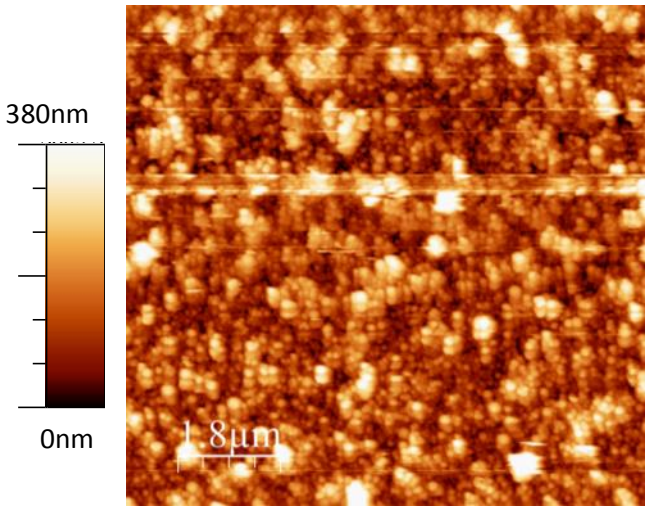

Figure 3.5) AFM micrograph of the sample with 20mm aggregation length.

Raman Spectra

Each Raman measurement lasted for 100 seconds for every sample using a 10% laser. For the reference measurements the measurement time was 120 seconds, but the laser power used this time was 0.1%. Figure 3.6a shows the measured Raman spectra of all three samples with different aggregation length, plus reference spectra (only glass). The 40mm aggregation length sample shows a high degree of crystalline Si, which is shown by the peak at 520 cm^{-1}.[63] The signal of amorphous Si is also present at 480 cm^{-1} and 150 cm^{-1} in all three samples.[64] Comparably with the 40mm aggregation length, 60mm aggregation length gave a sample with a higher proportion of a-Si. Using the 20mm aggregation length gave a crystallinity that is somewhere in between the other two aggregation length settings.

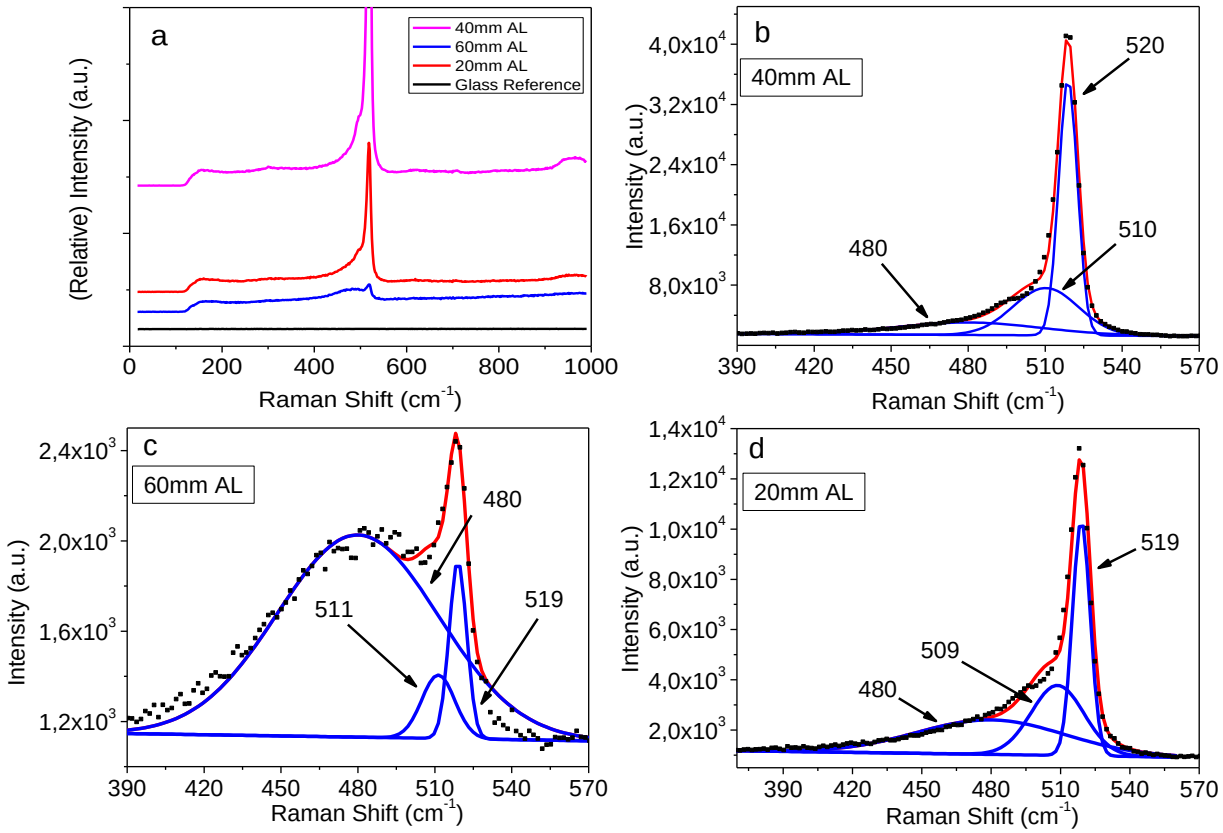

Figure 3.6a) Raman spectra of samples with 40, 60 and 20mm aggregation length and the reference glass substrate. De-convolution of the Raman peaks was carried out using Gaussian peaks. The result were different signals of the three peaks at 519 (c-Si), 480 (a-Si) and 509-511 (µc-Si) cm^{-1} position for samples with (b) 40mm aggregation length, (c) 60mm aggregation length and (d) 20mm aggregation length.

To determine the crystallinity, de-convolution of the peaks was performed by fitting 3 Gaussian peaks (µc-Si, c-Si, a-Si respectively) using XPSpeak 41 software. Figure 3.6b-c shows the result of the de-convoluted peaks per sample. The fits showed good agreement with the measured spectra in all samples, except for the 60mm aggregation length one. Fitting here showed reasonable agreement. The determined crystallinity, a-Si and µc-Si as well fraction are shown in table 3.4. It is shown that a 60mm aggregation length resulted in very little crystallinity. Interestingly, even if the crystallinity differed greatly from sample to sample, the ratio between the µc-Si and the c-Si remained roughly the same (0.4-0.46).

Aggregation length (mm)	Crystallinity, X_c	µ-crystalline fraction	Amorphous fraction, X_a
40	0.81	0.32	0.19
60	0.14	0.06	0.86
20	0.61	0.28	0.39

Table 3.4) Determined crystallinity for different aggregation length, as well as the a-Si and µc-S fraction.

UV-Vis for plotting Tauc plot of samples created with different AL

UV-Vis spectra were taken of samples with 20, 40 and 60mm aggregation length (figure 3.7). An attempt to calculate these spectra was done by using Lambert Beer's Law to calculate the absorbance for a-Si, µc-Si and c-Si at each wavelength using the absorption coefficient found in figures online and the film thickness for a-Si, µc-Si and c-Si determined with Dektak, respectively.[65,66,67] The film thickness are shown in table 3.5, 2nd column. Adding the calculated absorbance intensities of each a-Si, µc-Si and c-Si together gave the calculated spectra shown in the same three spectra of figure 3.7. It is assumed that the light absorbing species have no interaction with each other. The film thickness is also assumed to be uniform.

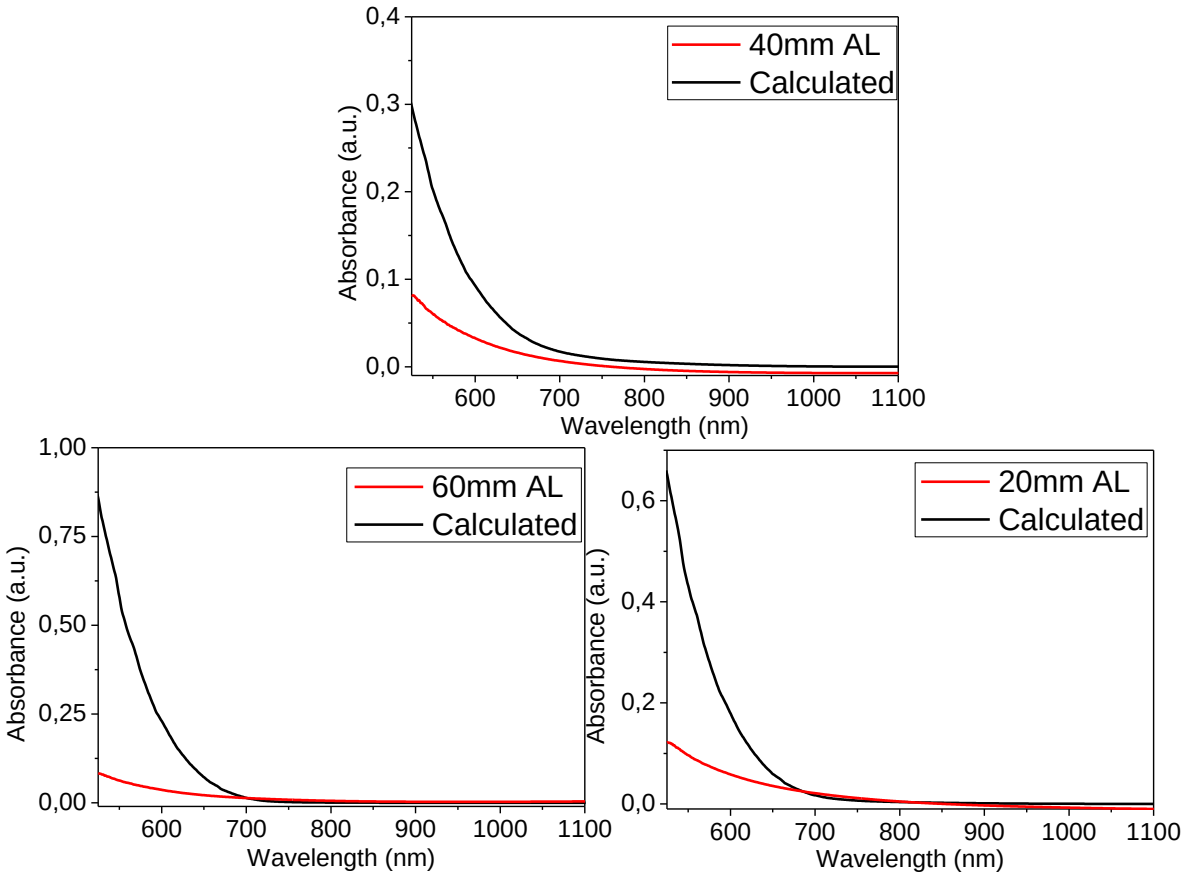

Figure 3.7) Measured UV-Vis absorption spectra of samples with different aggregation length (red line). Also UV-Vis absorption spectra were calculated shown in the same spectra (black line).

Aggregation length (mm)	Thickness (nm)	Band gap (eV)
40	92.5±14.8	1.58
60	86.6±15.0	1.47
20	88.4±22.1	1.4

Table 3.5) Thickness determined with Dektak (2nd column) and band gap determined with Tauc plot (3rd column).

The calculated spectra agreed reasonably with the measured spectra at long wavelengths, but not in the region with short wavelengths where absorbance is stronger. The absorbance seems to be overestimated in this region, which is explained by two reasons. Firstly, it is thought that the film is rather porous, so that the effective thickness is less than what is measured with Dektak. Factoring this effective thickness should give a lower absorbance in the region.

Tauc plots were made and shown in figure 3.8. An exponent of 0.5 and 2 was used to check which plot gave a linear plot. 0.5 yielded a better linear plot starting at low energies, which confirms a direct band gap. The energy band gaps for 40, 60 and 20mm aggregation length are shown in table 3.5, 3rd column. They appear to fall in or is near the range of a-Si reported in literature for a-Si (1.5-1.6 eV). C-Si has a band gap energy of 1.1 eV.[68] A-Si has a direct-like band gap as opposed to c-Si which has an indirect band gap. The plots are consistent with the Tauc plot method and the use of the 0.5 exponent is also used in literature for a-Si.[69] It is not clear why the sample with the 40mm aggregation length has such a high crystallinity, and at the same has the highest band gap. The results of both Raman spectra and Tauc plot do agree on the presence of a-Si. The standard error of the fit itself was not large enough to change the values with the number of reported significant figures. However, the error of the measurement with the instrumentation was not examined enough to be quantified, which could be significant and needs further investigation.

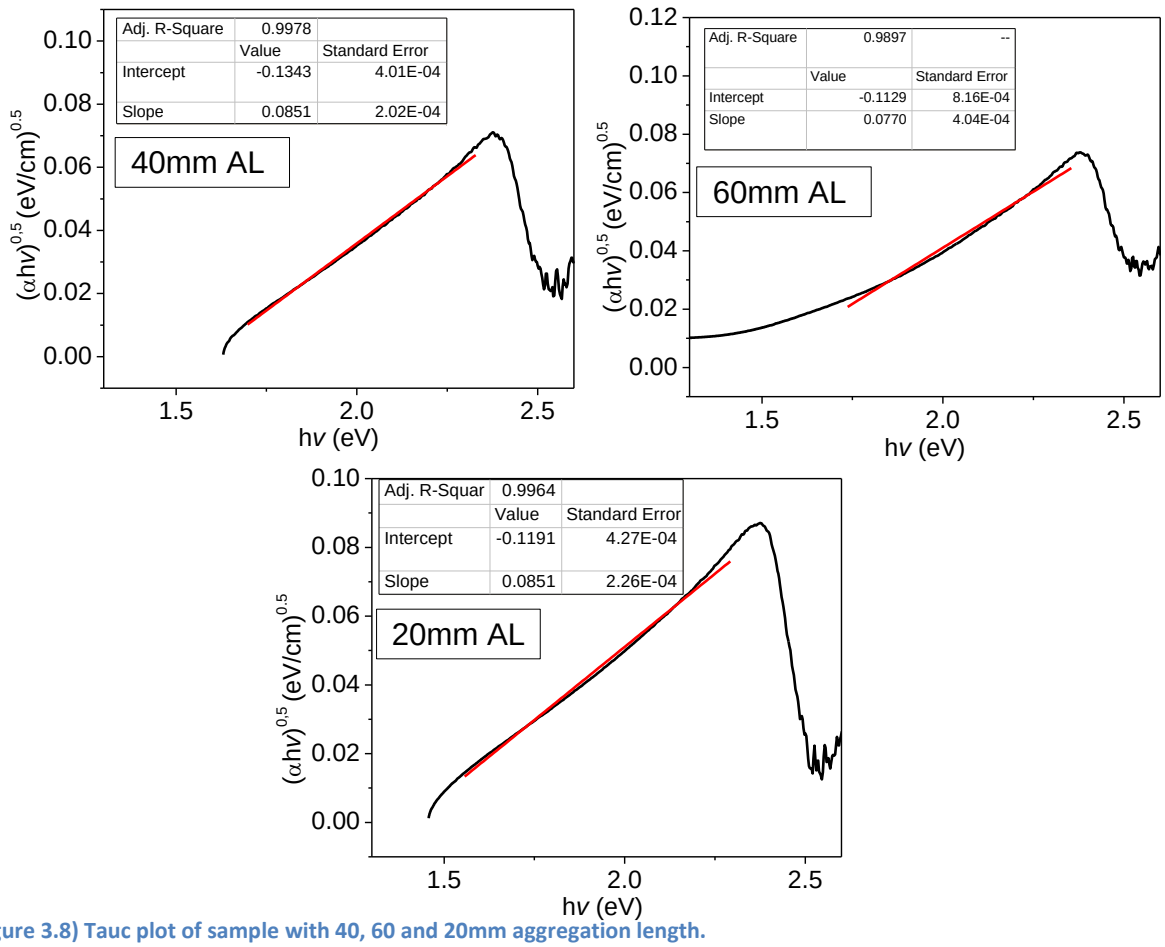

Figure 3.8) Tauc plot of sample with 40, 60 and 20mm aggregation length.

PL spectroscopy on different samples varying aggregation length

Photoluminescence (PL) measurements were performed on the experimental set-up 2 shown in figure 2.10 giving the emission spectra shown (excitation at 365nm) in figure 3.9a-e. A reference spectrum was taken of a clean glass substrate. A reference spectrum was also taken of a glass substrate with an a-Si layer sputtered for 15 minutes in a sputter chamber under low pressure conditions. The used parameters were 120 W magnetron power and 40 sccm Ar gas flow. The operating and background pressure were 1E-2 mbar and 3E-7 mbar, respectively.

The PL peak at ~475nm originating from glass has a long tail extending to 700nm. The ~425 nm "peak" in the same spectra is the result of the 418 nm wavelength filter being placed in front of the detector, as it covers a small wavelength range (~425-405 nm) that gradually decreases its transmittance of light before it completely blocks light of lower wavelength. An additional 380 nm wavelength filter was placed in front of the detector. This was used to block stray excitation light from reaching the detector and prevent higher order light diffraction. Nevertheless, the peak at 533nm seen in all spectra including the reference is caused by higher order diffracted light and originates from the excitation source. It is seen from the spectrum of the sample with aggregation length 60mm that it shows an additional rather sharp band around 515nm and a weak broad band around 630nm. These two bands correspondingly

overlap with the ones from the reference a-Si sample. The band at 630 nm is thought to be due to the recombination of electron and holes through defects in the oxide layer on the silicon layer that are also called surface states and is seen in a-Si. The ~515 nm peak was attributed to the luminescent recombination centres in a-Si. Comparing the position of this peak for the amorphous silicon with the ones from the samples, show that the peak is somewhat blue-shifted, i.e. 519nm vs 513 & 516 nm, respectively. This is presumably due to a size effect. It is important to keep in mind that the presence of μ-crystalline Si cannot be determined with PL spectroscopy, as it is only very weakly photo luminescent. Figure 3.10 shows a zoomed in view of the same spectra in figure 3.9 near the 630nm region. The shape of the 630nm peak in the reference a-Si spectra was compared to the spectra for the three aggregation lengths. There is a weak, but broad signal for a-Si in all spectra of samples with different aggregation lengths. From the a-Si reference spectra it is seen that the signal begins around 610nm and has a sharp cut-off for the signal around 650nm. That is also observed in the spectra of samples with different aggregation lengths. Furthermore, only a slight to no shift in the band is observed when comparing the samples with the reference. Time-resolved emission spectroscopy could give further insight on the 630nm signal.

Exciting at a slightly higher excitation wavelength would theoretically shift the higher order peak at 533nm to a longer wavelength and away from the PL peak at 515nm or disappear. A control experiment was taken that repeated the recording of spectra with excitation at 390nm instead of 365nm. The result is shown figure 3.11a-d. In these spectra it is confirmed that the peak at 533nm seen in previous spectra is a lower order diffraction effect originating from the excitation light as it is no longer seen.

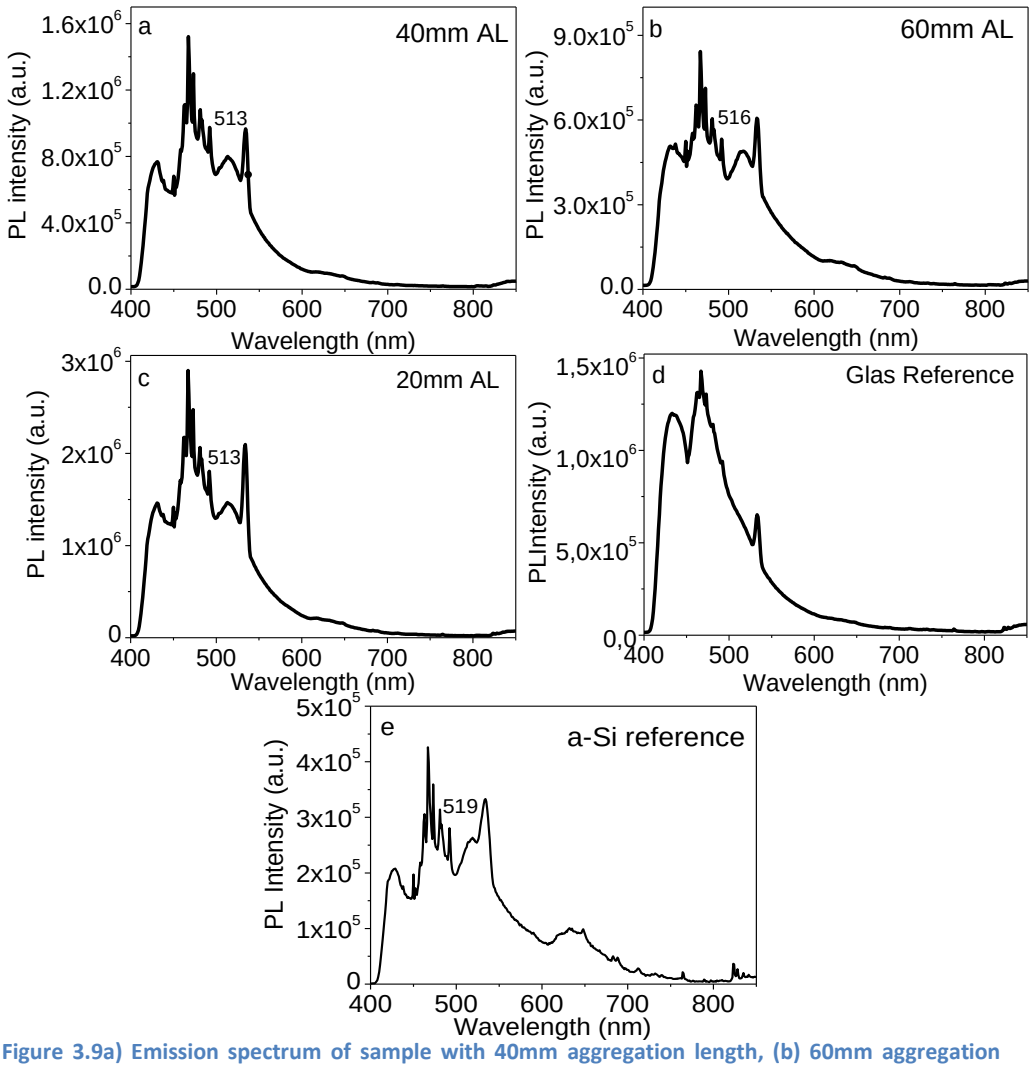

Figure 3.9a) Emission spectrum of sample with 40mm aggregation length, (b) 60mm aggregation length, (c) 20mm aggregation length,(d) Glass reference and (e) a-Si SS62. All samples were excited at 365nm.

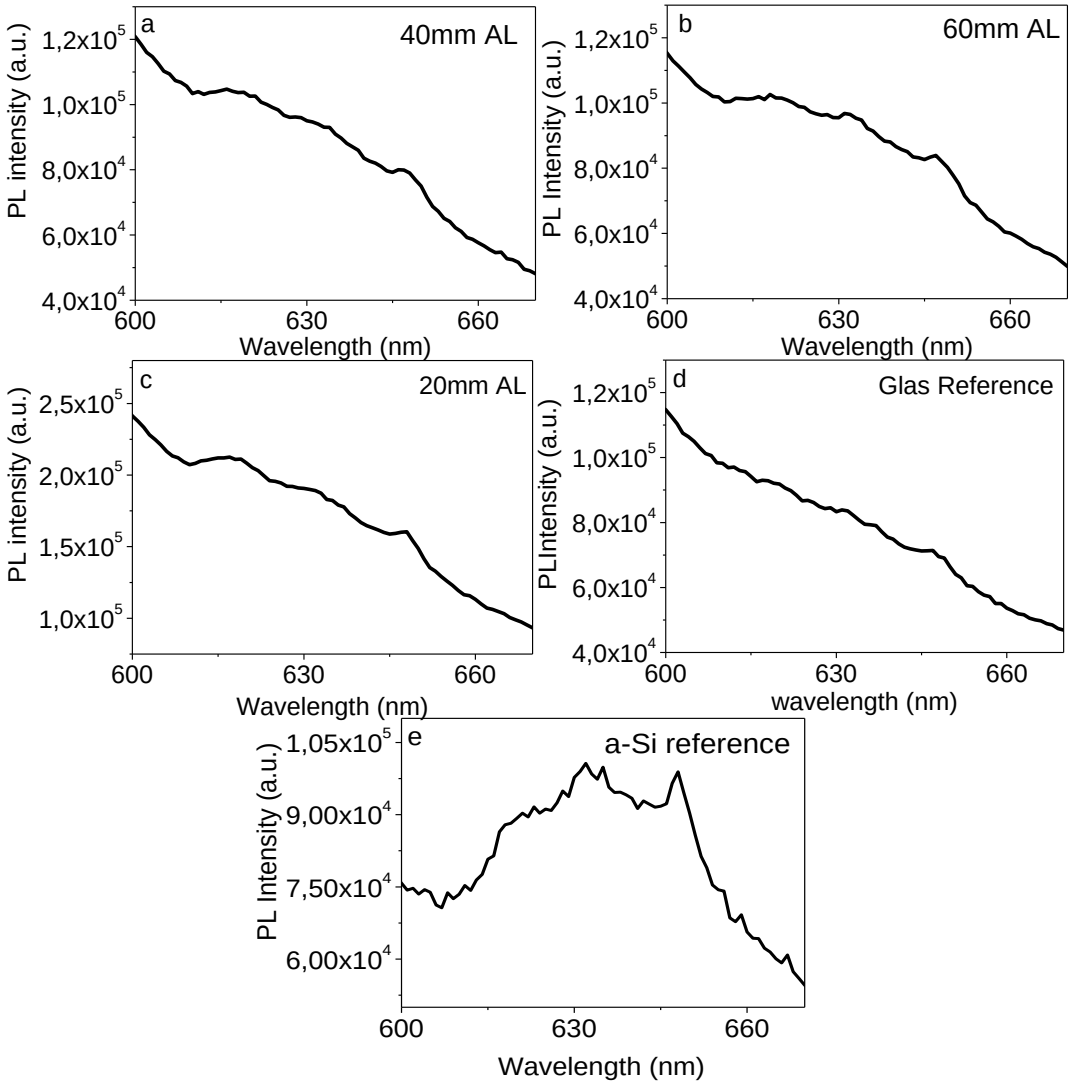

Figure 3.10a-e) Zoom-in of the spectra near the 630nm region of figure 3.9.

Figure 3.12 shows three emission spectra taken of samples that were made by depositing Si clusters on vacuum grease. Excitation was done at 365nm. The thin layer of vacuum grease was applied to glass beforehand. The cluster source parameters were kept the same as the samples in figure 3.9. The a-Si signal is stronger for the samples with 40 and 60 mm aggregation length, compared to their counterparts (depositions done on glass without vacuum grease in figure 3.9). The reason for this stronger a-Si signal is because of the higher sample / glass ratio. Apparently, Si clusters readily stick to the vacuum grease compared to glass. This difference caused by another substrate will be further discussed in a later section. The reason the sample with 20mm aggregation length on vacuum grease has a lower a-Si signal is thought to be due to sample loss during handling of the sample.

No consistent pattern in peak shift is observed in the different aggregation lengths, both for vacuum grease and glass substrates when figures 3.9 till 3.12 are considered. This may be due to a natural variability in the measurements. The largest expected peak shift is for when the excitation wavelength is changed from 365 to 390 nm.

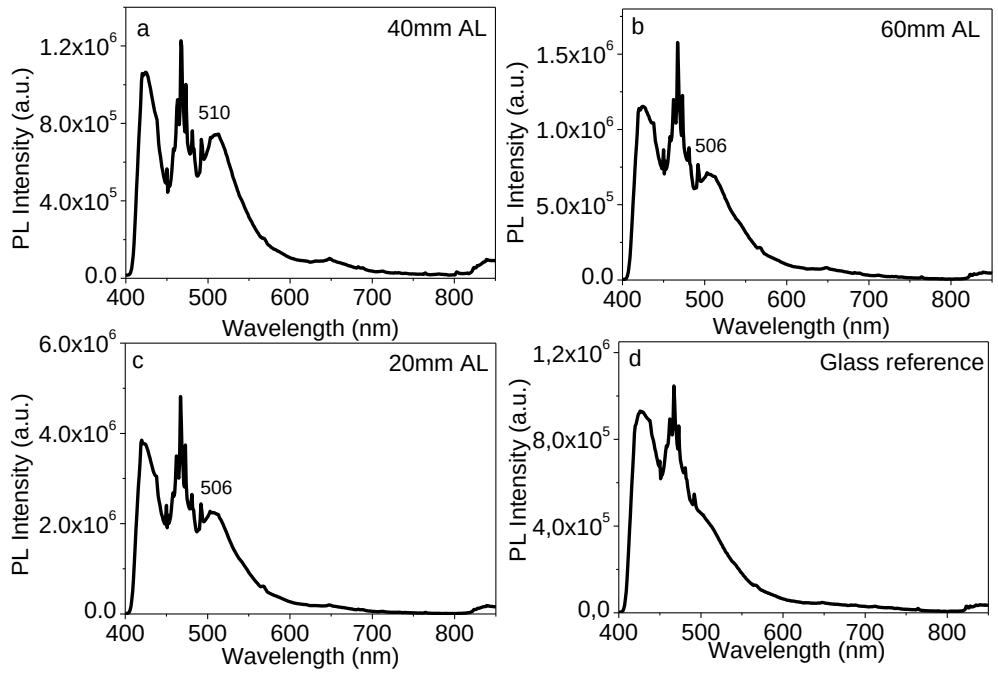

Figure 3.11a) Emission spectrum of sample with 40mm aggregation length (b) 60mm aggregation length, (c) 20mm aggregation length, (d) Glass reference. All samples were excited at 390nm.

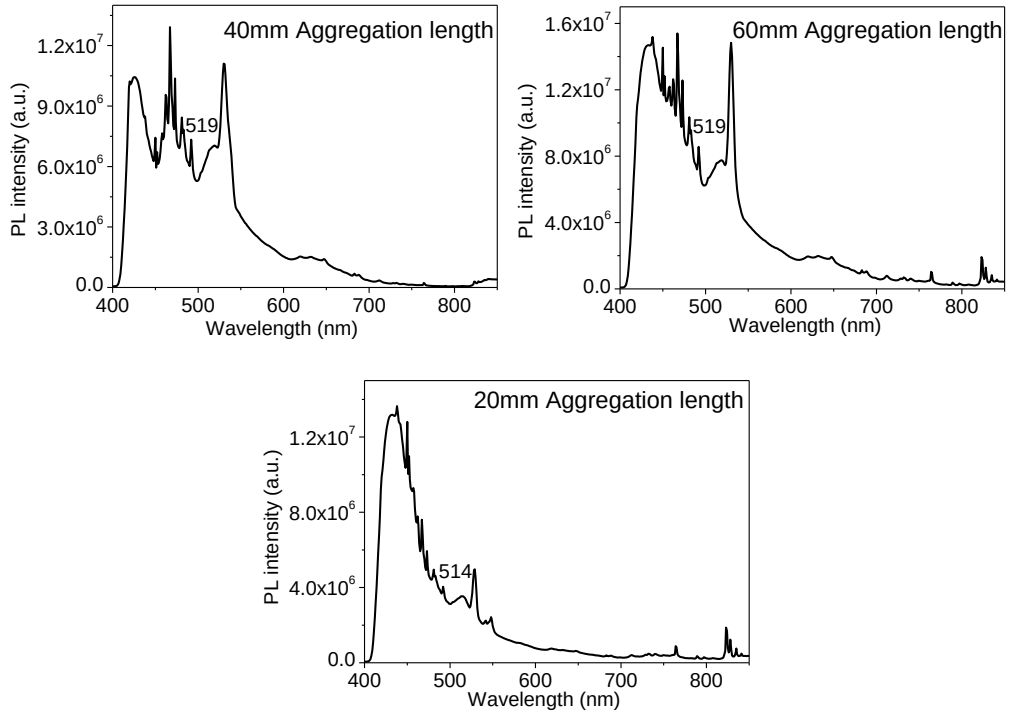

Figure 3.12) Emission spectrum of sample deposited on vacuum grease with 40mm aggregation length, 60mm aggregation length, 20mm aggregation length. All samples were excited at 365nm.

Excitation spectra

The samples with 20, 40 and 60mm AL were used to record excitation spectrum on the set-up 2 (figure 3.8a-d). The emission wavelength was kept fixed at 630nm. The excitation spectra shown in figure 3.13 indicate that the absorption tail begins at around 370nm. Reference and sample spectra are very similar in form. It was expected that the excitation at 365 nm would be absorbed more intensely. The weak absorption between 300 and 400 nm indicate to no quantum confinement that would otherwise increase light absorption of the clusters, and hence is more similar to the Si bulk form in this respect.

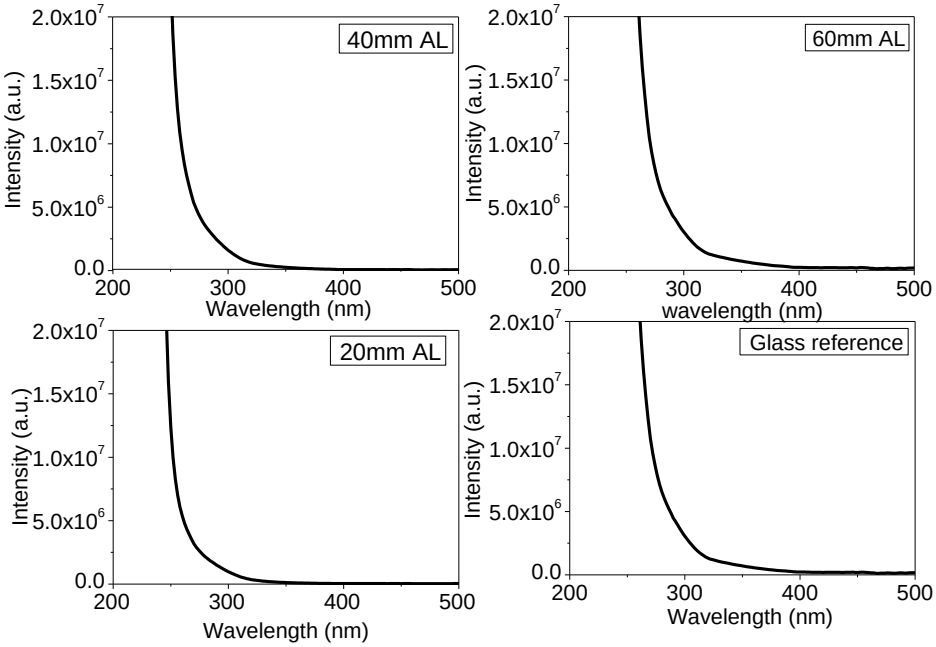

Figure 3.13) Excitation spectra of 40, 60 and 20mm aggregation length and glass reference. Emission wavelength was kept constant at 630nm.

Time Resolved Emission Spectroscopy

The decay time constants of the PL for the samples with 20, 40 and 60mm aggregation length was obtained through time-resolved emission spectroscopy. Firstly, a decay curve is measured by following the fluorescence response of a sample after a pulse of light is directed on the sample (The interval between the pulses was 50 ns) as a function of time measured at one wavelength. The measurements were carried out at 630 and 515 nm. These are shown in figure 3.14. Furthermore, a glass reference was also taken and all measurements used an excitation wavelength of 375nm. Bi-exponential fitting of the decay curves yielded slightly better fitting over mono-exponential fitting when the R-squared was compared (higher is better). The decay times and standard error, τ_1 and τ_2, are listed in table 3.6.

The τ_1 (630nm) was attributed to the detector response time, which was specified at 0.78ns at 0 ˚C according to the datasheet. The temperature sensitivity of the detector may be an explanation as to why some found τ_1 values deviated more from the manual specified response time than others. The recombination in a-Si seem to follow a fast decay time (5.3 ns) in the 40mm aggregation length sample and a slow one (17.3 ns) in the 60mm aggregation length sample, which suggests that the nature of recombination seem to differ between these two samples. No decay time constant was observed for

CS430 (AL 20mm) for the 630nm position and hence it also has no response time. The results of the Raman measurements showed an a-Si fraction for the 20mm aggregation length. A likely reason for this, is that the a-Si signal falls under the detection limit of the current set-up due to the low amount of sample material for the glass substrate. More sample material and thinner glass substrates should yield a stronger a-Si signal. Fast decay times in the 0.1-50ns was found in the literature for a-Si, which is in agreement with our results.[70]

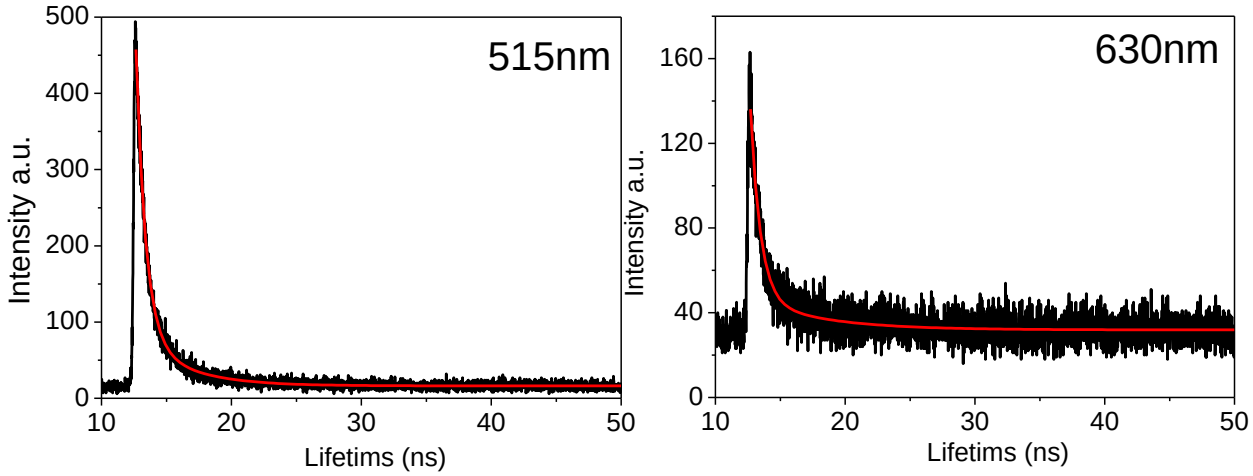

Figure 3.14) Bi-exponential fit of decay curve of the sample with 60mm aggregation length and measured at 515 and 630nm.

Aggregation length	τ_1 (515nm) (ns)	τ_2 (515nm) (ns)	τ_1 (630nm) (ns)	τ_2 (630nm) (ns)
40mm	0.51 ± 0.01	2.8 ± 0.1	0.47 ± 0.03	17.3 ± 3.1
60mm	0.75 ± 0.01	3.6 ± 0.1	0.76 ± 0.03	5.3 ± 0.7
20mm	0.36 ± 0.01	2.3 ± 0.1	-	-
Glass ref.	1.04 ± 0.03	5.4 ± 0.4	-	-

Table 3.6) Decay time constants, τ, determined at 515 and 630nm for the three samples with different aggregation lengths and reference. Results are obtained through bi-exponential fitting of decay curves.

The measurements were repeated with the samples that were made by depositions on vacuum grease. The measured wavelength was kept at 627nm. Figure 3.15 shows two decay curve measurements of the sample with 40mm and 60mm aggregation length using a laser pulse of 10µs. It is seen from table 3.7 that the decay times become substantially longer when the clusters are deposited in vacuum grease.

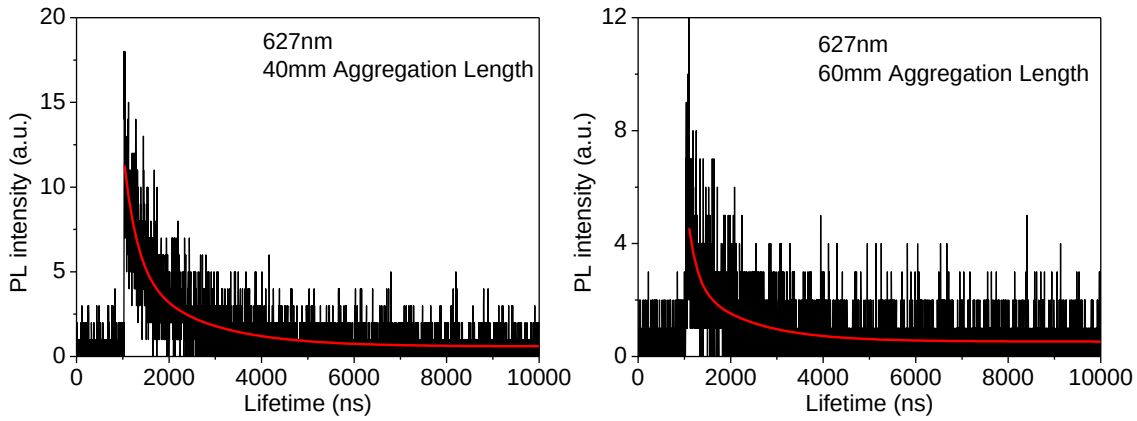

Figure 3.15) Bi-exponential fit of decay curve measured at 627nm of the samples deposited on vacuum grease. The 40 and 60mm aggregation length samples are shown (20mm aggregation length is not shown).

Aggregation length	τ_1 (627nm) (ns)	τ_2 (627nm) (ns)
40mm	191 ± 54	1256 ± 175
60mm	166 ± 16	1280 ± 84
20mm	292 ± 86	1483 ± 151

Table 3.7) Decay time constants, τ, determined at 627nm for the three samples with different aggregation lengths. Deposited on vacuum grease

TEM and High Resolution SEM (HR-SEM) imaging of investigated samples

To further study the effect of aggregation length on cluster formation using TEM, Si cluster depositions were performed on lacey carbon TEM grids using the settings listed in table 3.3 and a deposition time of 10 sec. The obtained micrographs with a Tecnai 12 (120kV) are shown in figure 3.16a-d. The first three pictures are three different samples that were made with a 40 (a), 60 (b) and then 20mm aggregation length (c). Figure d is a close-up image of figure b. Figure 3.17a shows relatively large particles of about 100nm and have different morphologies that are the result of some preferred direction for crystal growth leading to facets. The absence of small clusters of a few nanometre size, suggest that these have fused together without visible sign of their original, former shape. Figure b in contrast, shows larger spherical-like 'cauliflower' particles with a diameter of about 400 to 600 nm. These clusters exhibit no facetted particle growth, unlike those of in figure a. More importantly, the roughness of the clusters (see figure d) suggests that the constituents, i.e. the few nm-sized clusters have not lost their original shape entirely giving it a fractal-like morphology. Figure c also shows these cauliflower particles and what figure both b and especially c (close-up micrograph) demonstrate, is that these large particles can partially fuse together.

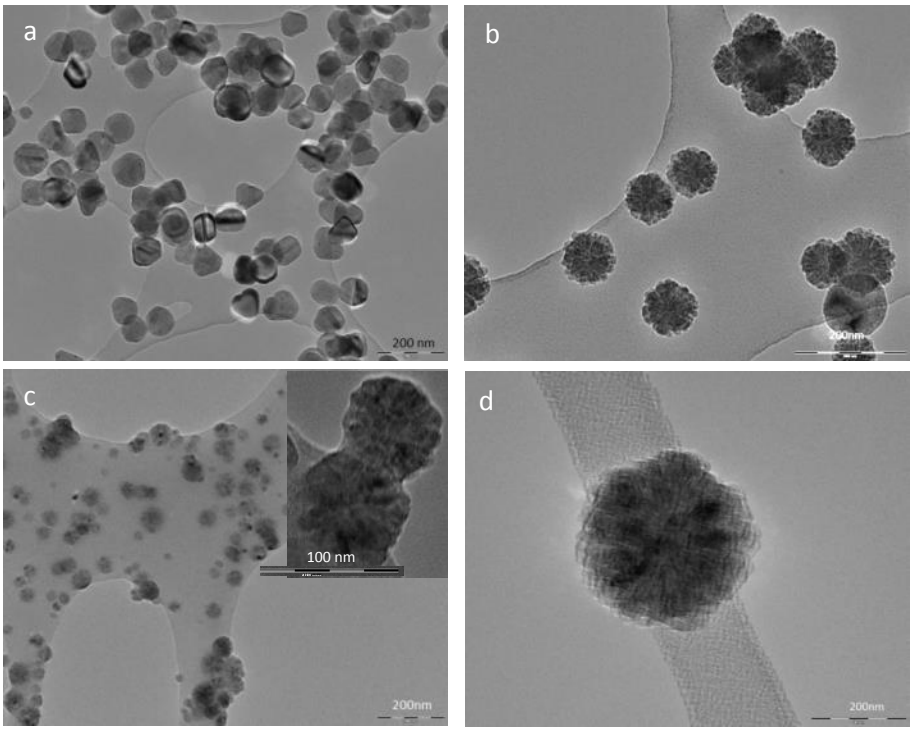

Figure 3.16a) TEM Micrograph of sample made with a 40mm AL, (b) 60mm AL, (c) 20mm AL and close-up image, (d) close-up image of 'cauliflower' particle of sample with 60mm AL. Scale bar included. All micrographs were taken with the Tecnai 12 (120kV).

The figure 3.16a-b high-resolution SEM (HR-EM) micrographs were taken with the Titan (300kV) for the sample created with a 60mm aggregation length. From figure 3.17a it is clearly seen that these cauliflower particles are comprised of fully (inside) and partially (outside) fused small clusters. The cauliflower particles reveal small regions of crystallites or grains, which are indicated with red circles in figure b. These regions reveal lattice structures with visible contrast that are stacks of atoms observed from above. The amorphous phase (circled with green) of is also observed to coexist between these

crystallites, which shows no clear contrast. Instead, it is shown as a combination of a white and grey blur.

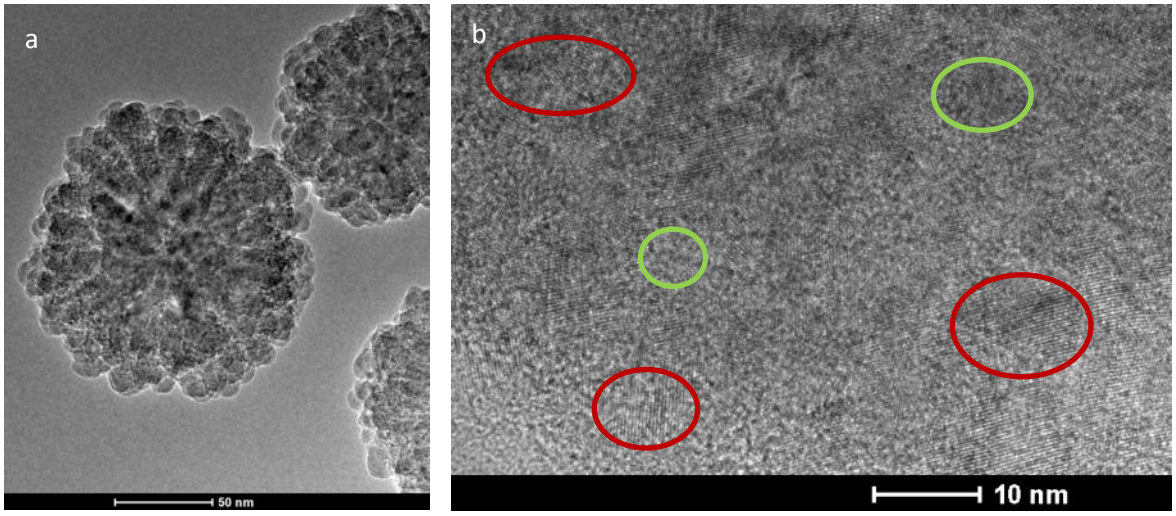

Figure 3.17a) HR-TEM micrograph of the 60mm AL sample and (b) close-up of cauliflower particle with crystallite region indicated with red circles, and amorphous region indicated with green circles.

HR-TEM images were also recorded of the sample with the 40mm aggregation length shown in figure 3.18a-b. A cauliflower-like particle is seen in figure 3.18a, which may be one of the few particles that is in transition between two forms, i.e. of a cauliflower particle (disordered) and a smoother particle with large crystal domains (ordered). The transition to a more ordered (facetted) particle is more stable thermodynamically, because of the energy minima obtained with a certain interatomic distance found in crystals. Additionally, the free surface energy is also reduced when the small clusters completely fuse with each other and form smooth particles. It is hence surprising that these cauliflower nano-particles are so long-lived seen for the samples with 20 and 60mm aggregation length, but a likely explanation for this state of matter is that it is meta-stable, i.e. a transition state.

In figure b a red arrow indicates the oxide layer, which is about 1-2 nm layer thick. The particle associated with this oxide layer also depicts a large homogeneous crystal domain alongside other particles with crystalline and an amorphous phase coexisting.

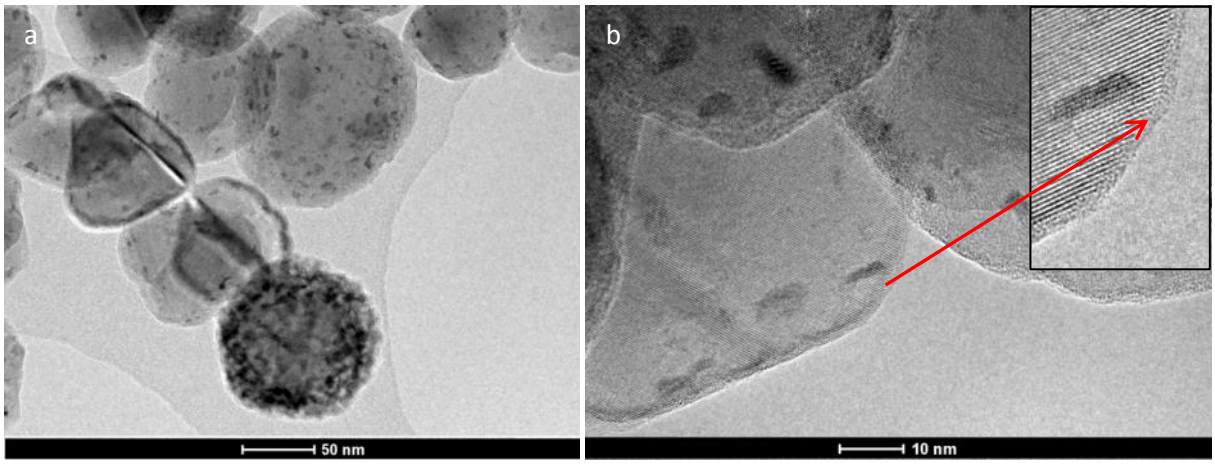

Figure 3.18a) HR-TEM micrograph of the 40mm AL sample and (b) further magnified image of different particles and close-up on the oxide layer.

High-angle Annular Dark-Field Imaging (HAADF), Secondary Electron Imaging (SE) techniques were also used to look at the cauliflower in detail (Figure 3.19a-b). SE-STEM allows three dimensional interpretation of the cauliflower particle, while HAADF is sensitive to the atomic number of the elements in the sample, so that the difference between elements can be seen as contrast. Oxygen (O-16) is a lighter element than Silicon (Si-28), so that the oxide layer should appear darker than the silicon core. The edges of the particle in fig 3.19a are sharper than in b, which seems to suggest that the oxide layer is hardly visible in a while it is well visible in b, and so confirming the presence of the oxide layer. However, the blurriness around the cauliflower particle in figure a could also be caused by the limitation of the detector, so that it is unable to have a sharp focus on the edges. Figure b shows that the cauliflower consists of smaller clusters.

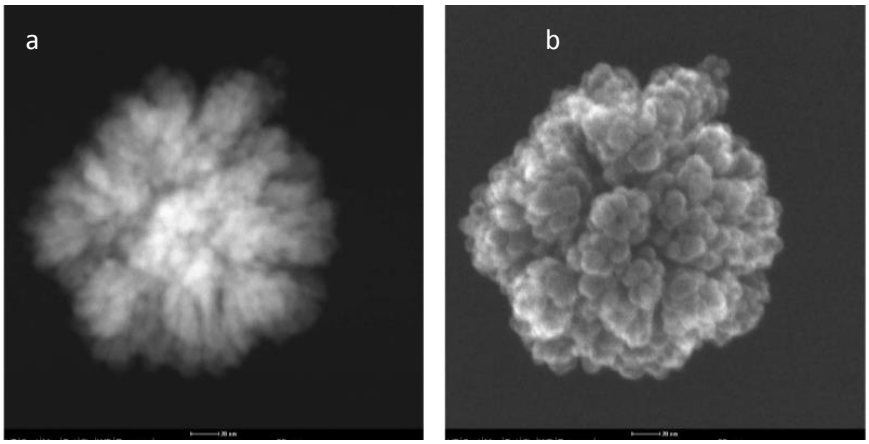

Figure 3.19a) HAADF-STEM micrograph and (b) SE-STEM micrograph of the sample

The sample plate was tilted in the Titan microscopic for several angles for each micrograph (figure 3.20). It shows several main branches that branch off from the centre. It also shows that the branch growth is isotropic (in all directions).

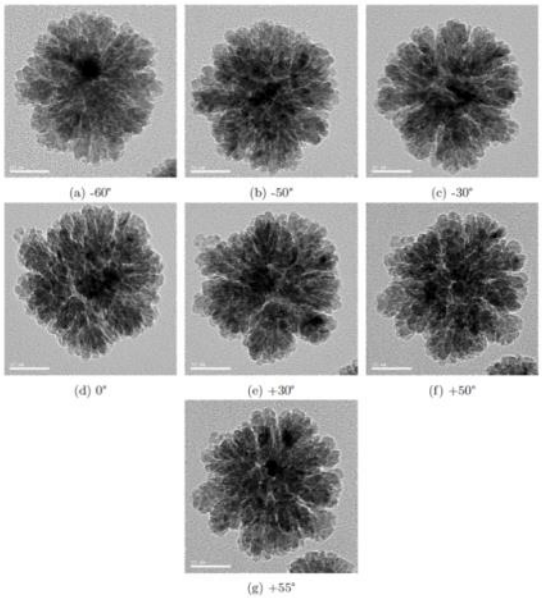

Figure 3.20) Tilt series of a cauliflower in the 60mm AL sample.

Crystal lattices extend periodically in all directions in crystals and form a diffraction grating for the electrons that interact through them. Electron diffraction is the technique that studies these diffracted electrons in a TEM microscope. The diffracted electrons fall upon a detector plate and are focused into bright white spots in a ring-like arrangement that are all around a central point on the captured image. Diffraction patterns yield information about the lattice parameters of the crystal and are characteristic of the material. The distance between the bright spots and the centre is inversely related to the interatomic distances of the lattice points.

An amorphous material with no long-range order would diffract electrons homogeneously around a ring, and thus form ring bands. Figure 3.21a-c depicts electron diffraction patterns taken with the Titan set-up. The sample in figure b (60mm aggregation length) shows clear band rings, which point to the presence of amorphous Si. Bright spots are also observed that indicate the crystalline phase. The homogeneous bands are softer in figure a and more clear peaks are shown and more peaks are visible in the outer rings. These observations are in line with the expectations from the samples seen in previous TEM micrographs and Raman results. Figure c (20mm aggregation length) shows pronounced bands and weak crystalline peaks, which suggests that the presence of the amorphous phase is dominant over the crystalline phase. That the 20mm aggregation length gave a higher amorphous fraction is in disagreement with the Raman result, which shows that the 60mm aggregation length gave the higher amorphous fraction. The result of the Tauc plot agree with the here presented results in that the amorphous phase is present.

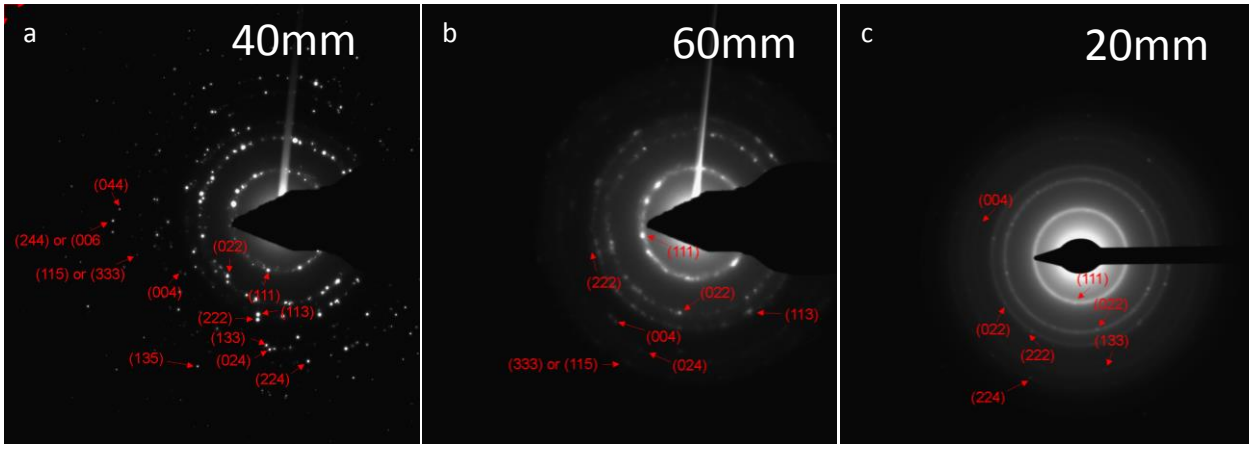

Figure 3.21a) Electron diffraction pattern of samples with 40mm AL and) 60mm AL that were taken with the Titan microscope and c) one taken of 20 mm AL with the Tecnai 12. Miller indices are assigned to the peaks.

The pixel distance from the centre to the first inner band, which also has the smallest radius was measured in iTEM. This radius is inversely correlated with the real d spacing, so it is also the largest spacing and is the (111) miller index with d spacing shown in table 3.8. This table shows the simulated d spacing of a Si cubic crystal.[71] The ratio between the first d spacing and the next d spacing have the same ratio as the ratio between the inverse pixel distance of the next and first band. Comparing the two ratios to check if they are the same is done to assign the miller index to each peak for each different miller index. The (002) miller index was not observed. This is likely, because of the diffracted electrons destructively interfering with each other.

Miller index	d spacing (Å)
(111)	3.135416
(002)	2.715350
(022)	1.920042
(113)	1.637418
(222)	1.567708
(004)	1.357675
(133)	1.245888
(024)	1.214341

Miller index	d spacing (Å)
(224)	1.108537
(115)	1.045139
(333)	1.045139
(044)	0.960021
(135)	0.917956
(244)	0.905117
(006)	0.905117

Table 3.8 Miller indices and d-spacings for Silicon.

The relation on how the Aggregation length influences the formation of these two different kinds of particles is much related to the distance=time that aggregation of the clusters inside the chamber can occur. What is known from the TEM results is that the 40mm aggregation length heavily favours the creation of more crystalline and smoother particles, a 20mm aggregation length favours the formation of amorphous, cauliflower particles and 60mm aggregation length is somewhere in between.

Addition of oxygen after depositing Si clusters

An oxygen gas cylinder was attached to the central chamber via a mass flow controller. This configuration allowed a controlled oxygen flow rate directly in front of a sample after a deposition. The aim was surface passivation of the Si clusters by creating SiO_2 groups as to form a barrier to prevent the small clusters from coalescing. An oxygen flow of 2.74 sccm was used and the operating pressure was 1.6E-3 mbar. Table 3.9 shows the samples that were created with different settings on a glass substrate using the same cluster source parameters as CS341. Each deposition is followed by an O_2 flow, and subsequent next deposition. This was repeated under identical conditions. Using the previous procedure, histograms were made shown in appendix B. Subsequent statistical analysis (sampling size +50 clusters) yielded the results shown in the last three columns. One complicating factor in determining the surface cluster density was the close proximity between clusters and some partially fused clusters. Therefore, the calculated density should be taken as a lower limit.

A positive correlation between the deposition time before each oxygen passivation step and the mean cluster size was observed. A shorter deposition of 10 to 20 seconds time gave smaller clusters on average compared to the longer deposition time of 30 and 60 seconds. Figure 3.22a-b show that the coalesced clusters stick together. Furthermore, figure 22a marks a group of large clusters that have a structure, as opposed to a smooth surface that one would expect of a spherical cluster. This structure seems to consist of smaller clusters as was already shown by the TEM results. The observation of two size distributions of cluster populations in the CS377 histogram shown in figure 3.22, one centred at ~40nm and the other at ~95nm (although there are clusters larger than 160nm), suggest that the smaller clusters are still in the process of coalescing to form larger clusters when the deposition is stopped after ~10 s. The subsequent oxygen flow passivation step prevents some clusters from coalescing before the next deposition. When a deposition time of 20 sec is taken as in sample CS376, the histogram demonstrates that the two cluster populations are coalescing and forming a single sized cluster population. The smaller clusters are more mobile over the surface which are more likely to coalesce. This is less likely for large clusters. The results point that the attempt preventing the clusters from coalescing with oxygen addition on the surface failed.

Sample number	Dep. time (s)	O_2 flow duration (s)	Freq.	Total dep./ O_2 flow time (min)	Sample size	μ_1 (nm)	μ_2 (nm)	σ_1 (nm)	σ_2 (nm)	Cluster density (10^8/cm^2)
CS372	30	60	6	3 / 6	75	85.5	-	22.7	-	100
CS373	60	60	3	3 / 3	59	92.5	-	24.3	-	111
CS374	60	120	3	3 / 6	55	90.0	-	26.8	-	130
CS375	60	30	3	3 / 1.5	61	79.3	-	21.1	-	139
CS376	20	60	9	3 / 9	55	60.2	-	25.5	-	97
CS377	10	60	9	1.5 / 9	54	40.0	106	30.7	48.7	92

Table 3.9) Si cluster deposition followed by an oxygen flow, which is then repeated (frequency). These were varied and then statistical analysis was performed to determine the mean cluster size, standard distribution and cluster density.

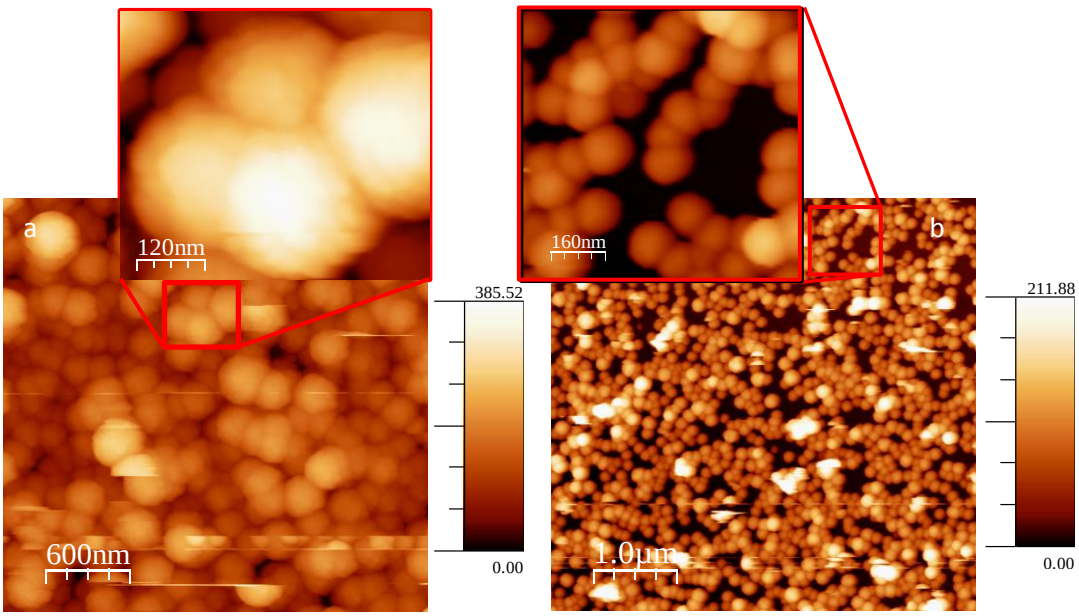

Figure 3.22a) Micrograph of sample CS377 and magnification on large cluster. (b) Micrograph of sample CS373 and magnification on cluster structures. Scale bar is in nm.

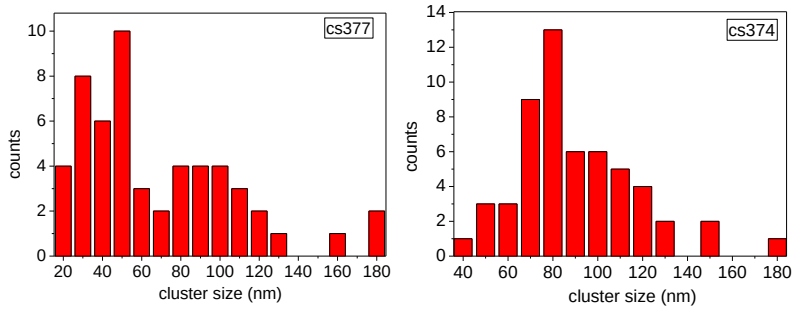

Figure 3.23a) CS377 and (b) CS374 histogram of cluster size diameter.

Deposition on different substrates using a copper wire mesh front

The effect of charge and substrate on the Si cluster deposition was also studied. A copper mesh was cut and cleaned in iso-propanol in a similar manner as the cleaning step of glass substrates. This copper mesh was then fixed right in front of the Si wafer or glass substrate in a sample holder, so that the surface of the mesh and the substrate are in contact (figure 3.24a). Si clusters deposition were deposited using CS341 parameters for 3 minutes on both samples CS355 (Si wafer) and 356 (glass). The result is shown in figure 3.24b and c.

The mesh structure has a significant effect on the positions where the Si clusters are deposited. The Si clusters have settled to a high degree underneath where the copper mesh wires were fixed to a significant degree. AFM confirms this for the Si wafer (b), as the visible lines are formed by large aggregated clusters 60-120 nm and are packed more densely, compared to the areas in between the wires that have considerably less cluster density, but comparable cluster size. The glass substrate (c) shows some common features with the Si wafer (b). What they have in common is that the Si clusters again prefer to reside underneath the mesh structure due to a Coulomb force. This effect in both cases happens, because of the high surface mobility of the clusters on the surface. Clusters can get trapped underneath the copper wires when they touch. This leads to a local snowball effect as other clusters diffuse to the trapped clusters under the wires and coalesce. This does not happen everywhere underneath the copper wires for Si wafer. It is likely that the contact area between the wires and the surface was not as good in those sections as the reason. It is possible that positively charged clusters have their charges neutralized when they get under the copper wire, as the wire is grounded. These charged clusters display a behaviour to preferably reside under the wire.

The surface diffusion also leads to the clusters to gather underneath the section of the surface that was covered by the metal sample holder. For the glass substrate this seems to happen to a lesser degree. The more uniform Si wafer surface has relatively few surface defects that allow less impediment to surface diffusion compared to the glass surface. The encounter of a step in the surface is an example of an intrinsic defect that can trap clusters.[72]

Ag clusters were produced by DC sputtering of a Ag target in vacuum. A voltage, current Ar flow and deposition time of 269 V, 1.09 A, 20 sccm and 3 minutes were used, respectively. Depositions were performed on a Si wafer and glass substrate with a copper mesh similar to what was done for Si clusters (figure 3.24d-e). Firstly, it can be observed that Ag clusters on Si wafer behave differently by not diffusing to the section of the surface that is under the sample holder. This is also seen for the glass substrate. This can be attributed to a lower mobility of the clusters due to a relatively strong cluster-surface interaction. Strikingly, the clusters are also observed to be absent from underneath the copper wires, whereas the opposite was seen for the Si wafer. The difference in mobility is what causes these patterns. Theoretically, one can exploit this effect by carefully picking out a substrate to create patterned thin lines. Alternatively, positively charged Ag clusters are highly conductive even when the charge is neutralized. Since the surface is covered by Ag clusters and grounded, Ag clusters do not settle under the copper wire. The cluster sizes are similar to that of the Si clusters.

A point that remains unaddressed is the discrepancy of the surface coverage between the glass and Si wafer. Less clusters stick to the Si wafer than on the glass substrate even though they use the same parameters. The sticking coefficient, the number of clusters that stick to the surface divided by the total number of surface collisions by the clusters, is thus higher for glass and which it is thought to be due to its rougher surface.

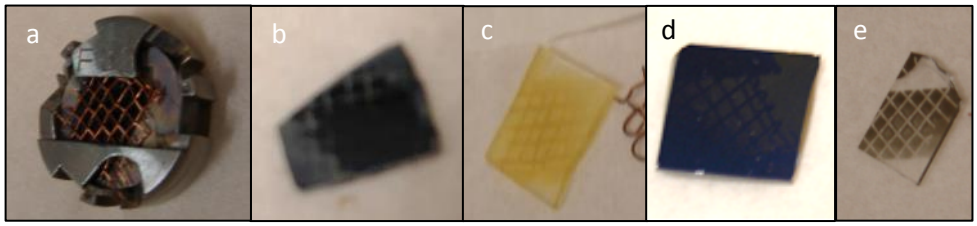

Figure 3.24a) Si wafer with copper wire mesh front held together in a sample holder. (b) Sample Si clusters on Si wafer substrate (CS355) (c) Si clusters on glass substrate (CS356) (d) Ag clusters on Si wafer substrate (CS385) (e) Ag clusters on glass substrate (CS386). All samples had a copper mesh front.

When a thin layer of vacuum grease was applied to the surface of glass in a rather using no copper mesh and followed by a Si deposition of 2 minutes using the optimal settings, a thick brown layer of Si was observed shown in figure 3.25a. That demonstrates that vacuum grease has a very high sticking coefficient for Si clusters.

Interestingly, it was found that a 5 minute Si depositions on ITO (no copper mesh) that was electrically isolated had a significant effect on the adherence of the Si clusters, compared to not electrically isolating the substrate. More specifically, if there was a measured conductivity between the metal sample holder and the ITO substrate, the Si clusters were far less likely to adhere to the surface. Electrically isolating tape was used on the edges of the surface, so that there was no electrical pathway between the sample holder and the ITO. The result of the deposition is that it does lead to more cluster adherence to the surface (figure 3.25b-c), but a complicating effect is that the layer is not homogeneous, i.e. some samples have patches of Si layer and leave the rest of the surface with little clusters. Since the clusters are charged before landing, the grounding affects the acceleration or decelaration of the clusters and thereby affects the sticking of clusters on ITO. This effect differs significantly for every sample as can be observed when comparing figure b with c. Ordering the substrates according to their sticking coefficient from high to low: Vacuum grease > glass > Si wafer/ITO (not electrically isolated).

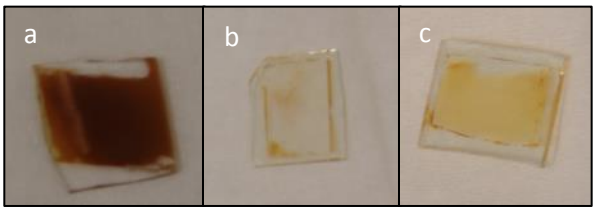

Figure 3.25) Deposition on vacuum grease (CS378) (a) and ITO (b & c). Note the clean edges of the samples where there was electrical tape (b & c).

Si depositions on ITO, silver evaporation and the Solar Simulator

An effort was made to create individual solar cells by evaporating silver on Si layer for numerous samples by using a mask for different aggregation length (60, 40 and 20mm). The IV-curves were then measured with a solar simulator under dark and AM 1.5 conditions shown in figure 3.26a-b.

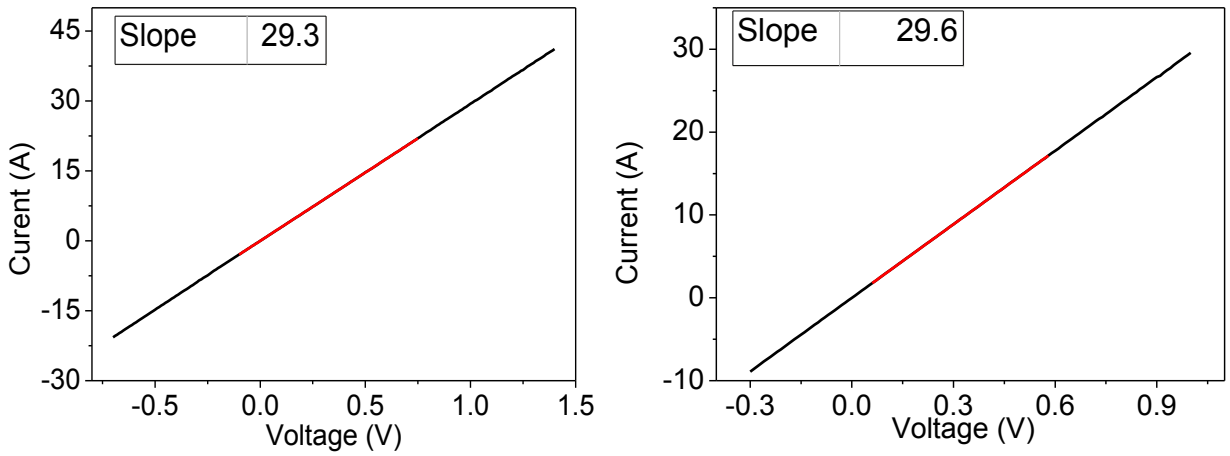

Figure 3.26a) IV-curve of the same sample with linear fit to determine the slope under dark (left) and AM 1.5 conditions (right).

The samples showed a linear response under both dark and AM 1.5 conditions. The response indicate a short-circuit of the samples. Two likely reasons for this are that the electrode probe penetrates the thin Si layer and that some very small dust particles were observed on the substrate. The latter shows that working in dust free environments and a thorough cleaning procedure is important for making solar cells. One solution for the excessive force of the electrode mounting problem was to use silver paint to apply it together with a thin copper wire. This copper wire would prevent the electrode from destroying the solar cells. Figure 3.27 shows one sample with one solar cell that seems to have no flaw, but likely short-circuited due to a tiny dust particle.

Figure 3.27) Silver conductive layer (white) added to Si layer (yellow) deposited on ITO.

Discussion of Results

Numerous depositions and subsequent analysis reveal that a variety of Si cluster species have been made. Figure 3.28 shows a schematic for how these species evolve in different stadia. First, a cloud of Si atoms nucleate and then grow together to form small clusters of a few nm. AFM micrographs of Si clusters deposited on Si wafers shows that these small clusters that are in the quantum confinement region due to their size, which is a few nm. Depositions on glass using the same parameters subsequently revealed that firstly, more clusters are deposited on glass as compared with the Si wafer, and secondly, the small clusters can diffuse over the surfaces as such that they can stick together to form aggregates. Raman spectra and electron diffraction patterns are in agreement that the aggregation length does determine the crystallinity of the sample. HR-TEM further reveals that the 40mm aggregation length is capable of creating crystallites of about 50-100nm, while a 60 mm aggregation length creates cauliflowers that consist of both small regions of crystalline and amorphous silicon. This is thought to be an intermediate state, and so in terms of stability is in between that of a-Si and c-Si, with c-Si being the most stable. The close spacing of the small regions of crystalline and amorphous silicon could be the reason why there is no quantum confinement. An aggregation length of 20mm creates amorphous clusters that can also form cauliflowers. The absence of these cauliflower particles in the case that the crystallinity is high suggests that the disordered structure of a-Si plays an important role.

Results of the Raman data, Tauc plot from optical absorption, and electron diffraction patterns all agree in the respect that there is a-Si, although only Raman and the electron diffraction patterns managed to prove the crystallinity in the samples. The point on which the electron diffraction pattern and the Raman result disagree, is on whether the 60 or 20mm aggregation length is more amorphous. It is not clear which reason causes this discrepancy exactly, but it might be that the different substrate played a role in causing this difference. PL spectra showed a weak a-Si PL that is present in all samples, and no significant or consistent shift in peak that might due to quantum confinement of Si clusters was observed. This is in agreement with observations that the small Si clusters have coalesced to larger clusters on the surface observed with AFM. Furthermore, excitation spectra show no increased light absorption between 300-400nm, and the spectra were more similar to the bulk form of silicon.

No decay time was found for an aggregation length of 20mm, which was blamed on the low sample material. Longer decay times were found for a-Si deposited in vacuum grease than when they were deposited on glass with a magnitude of 2 or 3 of difference. Non-radiative recombination is thought to be reduced due to the limited movement of charge carriers and excitons. Aside from the 20 mm aggregation length, the results from the Tauc plot, the Raman spectra and electron diffraction pattern agree with the time-resolved emission spectroscopy result on the presence of amorphous Si in the 40mm and 60mm aggregation length. The results are summarised in table 3.10. Other results were also found, namely that the oxidation step failed to prevent coalescence after deposition of Si clusters with some limited success in creating slightly smaller clusters doing a short deposition before oxidation. Another method needs to be devised to prevent this problem. One idea is to embed Si clusters in a sputtered layer, and to repeat this procedure in order to create thicker films.

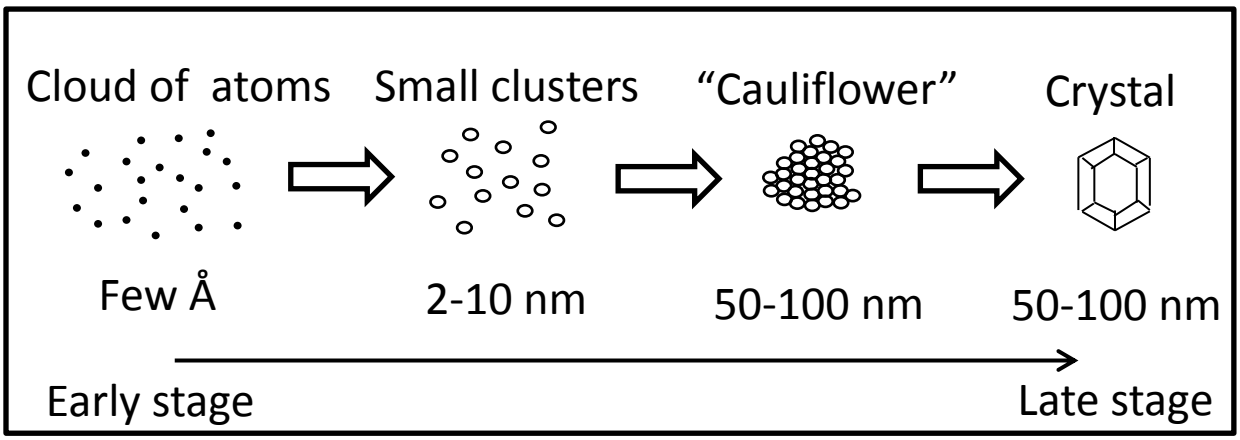

Figure 3.28) Evolution of the different stages for Si starting in the cluster source.

Technique used	40mm Aggregation length	60mm Aggregation length	20mm Aggregation length
Raman	+/-	+/-	+/-
UV-Vis	+	+	+
PL (+ TRES)	+ (+)	+ (+)	+
Electron diffraction pattern	+/-	+/-	+/-

Table 3.10) Results for the different techniques used for the samples with different aggregation lengths. “+” means a-Si was detected with the technique. “-“ means c-Si was detected with the technique.

Conclusions

Si nanoparticles were produced with the gas phase aggregation cluster source by using a set of parameters that yielded clusters with a large amount in the quantum confinement region. AFM revealed that the Si QDs aggregate during production and also can further coalesce after deposition. TEM/HR-TEM showed that small Si particles aggregated into 'cauliflower' particles which in a next step can turn into facetted crystallites. Furthermore, Raman and HRTEM reveal that these 'cauliflower' particles consist of both, amorphous and crystalline silicon phases. The close proximity of the nm-sized crystalline and amorphous regions can be a reason why there is no quantum confinement in the 'cauliflower' particles. Photoluminescence spectroscopy showed a weak a-Si signal, and optical absorption spectroscopy confirmed a-Si in all samples. Silicon nanoparticles deposited unto vacuum grease displayed much longer decay times than when it is deposited unto a glass substrate. Another reason for not observing quantum confinement effects are due to the large size of the nanoparticles. Deposition on different conductive and non conductive substrates showed a clear dependence on the amount of deposited clusters and conductivity. This work is a first step in creating and characterising Si nanoparticles produced with the cluster source, with the purpose of eventually applying this to solar cells.

Acknowledgements

This thesis could not have been written without the support and help of the following people. Special thanks go to my supervisor, Marcel for making this project possible in the first place. Your expertise and professionalism inspired me to be a better researcher and learn more. Thank you, Marijn, for taking the stunning HR-TEM micrographs, electron diffraction patterns and TEM micrographs. Many thanks go to Andries for being so kind to let me use the Eddy 1 and Eddy 2. Thanks go to Joren for being very helpful for setting up the PL/TRES measurements as well as the excitation spectra, and finally for answering all of my questions. My gratitude goes to Wessel for taking the first TEM micrographs of the cauliflower particles. I would also like to thank Wiebke for instructing me on how to use the UV-Vis spectrometer. Credit goes to Maarten at ECN for measuring the Raman spectra of my samples on two occasions. I would like to thank Veronique at ECN for giving me instructions on how to use the Dektak Profiler. Thanks, Marc from CMI for giving a detailed explanations on how to use the AFM and help with me any AFM problem. I very much appreciate the nice HAADF/SE images you took, Da, thank you. Last, but not least, thank you, Fabian for taking TEM micrographs of my newest samples.

Appendices

Appendix A

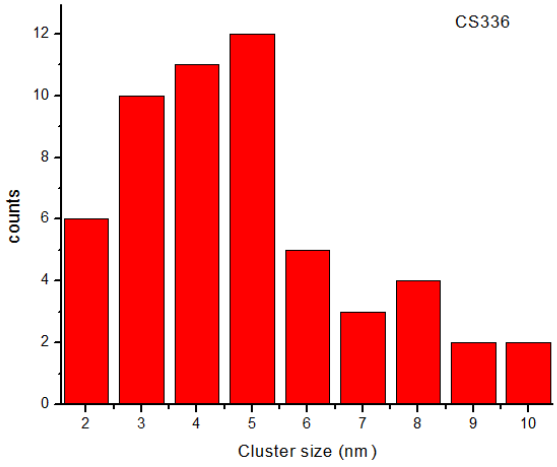

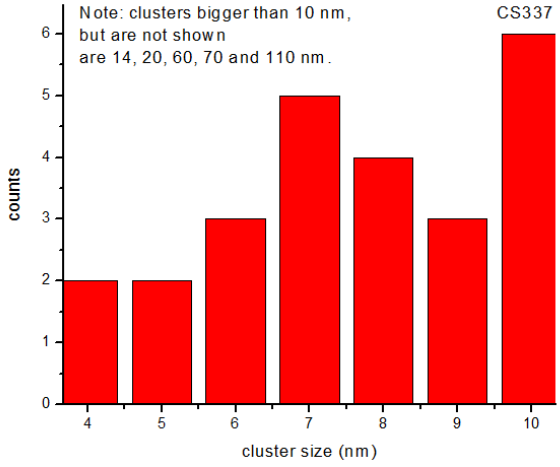

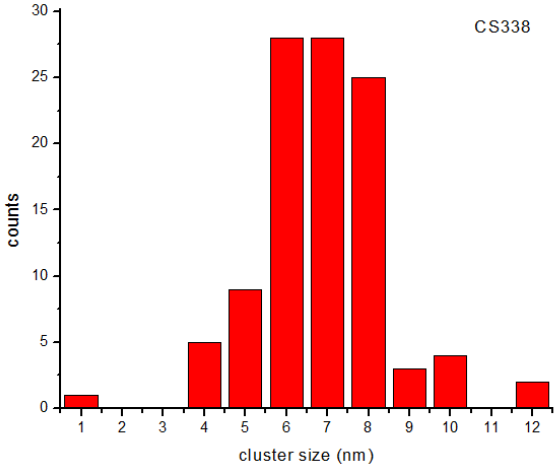

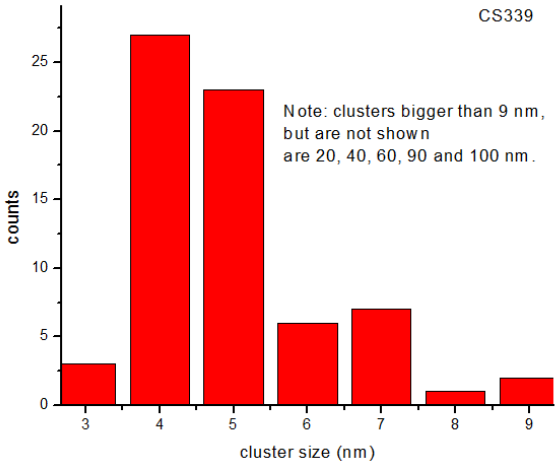

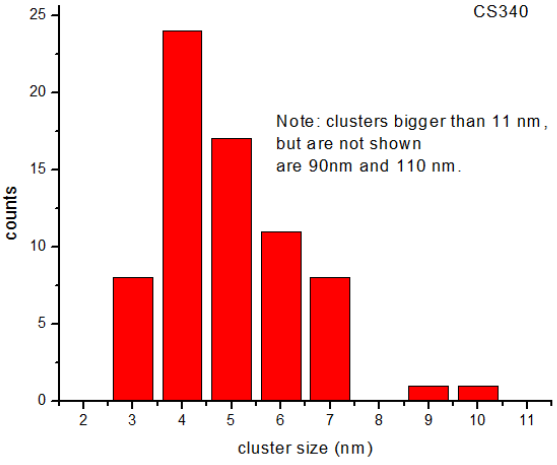

Appendix B

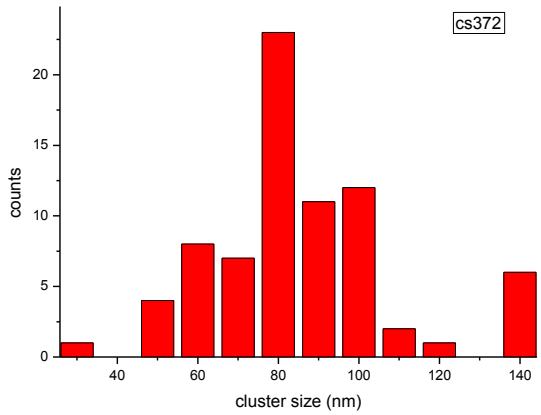
cs372
counts
cluster size (nm)
0
5
10
15
20
40
60
80
100
120
140

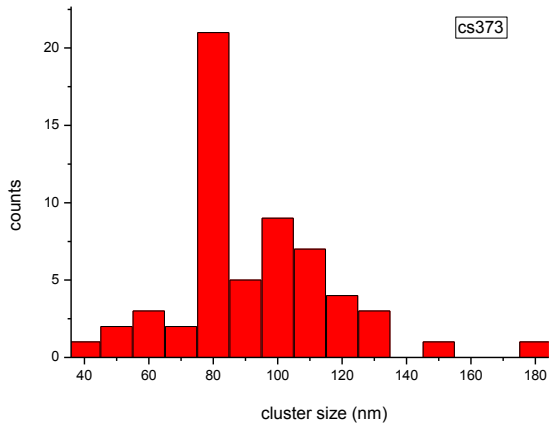
cs373
counts
cluster size (nm)
0
5
10
15
20
40
60
80
100
120
140
160
180

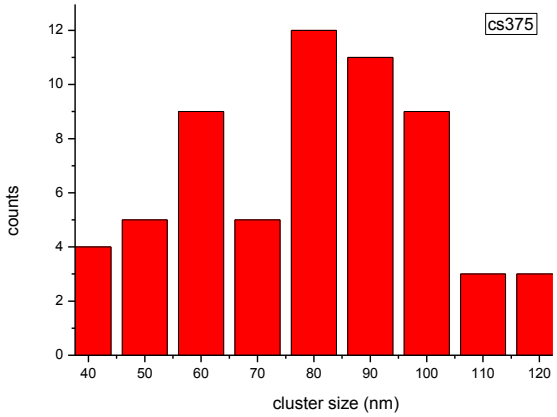
cs375
counts
cluster size (nm)
0
2
4
6
8
10
12
40
50
60
70
80
90
100
110
120

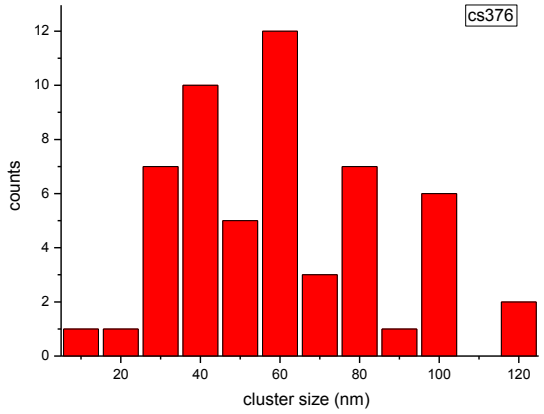
cs376
counts
cluster size (nm)
0
2
4
6
8
10
12
20
40
60
80
100
120

References

[1] D.E. Carlson, C.R. Wronski, *Amorphous silicon solar cells,* Topics in appl. Phys. **36,** 287 (1987)

[2] S. Tatsuo, *Advances in crystalline silicon solar technology for industrial mass production*, npg asia mater. **2**, 97 (2010)

[3] Gaëtan Masson, *PVPS Report Snapshot of Global PV 1992-2013,* EPIA, p. 6+13 (2014)

[4] S. Tatsuo, *Advances in crystalline silicon solar technology for industrial mass production*, npg asia mater. **2**, 98 (2010)

[5] S. Tatsuo, *Advances in crystalline silicon solar technology for industrial mass production*, npg asia mater. **2**, 99 (2010)

[6] F. Priolo, *Silicon nanostructures for photonics and photovoltaics*, nature nanotech. **9**, 26 (2014)

[7] TU Delft OpenCourseWare, Solar cells syllabus Chapter 4, http://ocw.tudelft.nl/courses/microelectronics/solar-cells/readings/, 4.4 (visited 15-3-14)

[8] S. Tatsuo, *Advances in crystalline silicon solar technology for industrial mass production*, npg asia mater. **2**, 98 (2010)

[9] TU Delft OpenCourseWare, Solar cells syllabus Chapter 4, http://ocw.tudelft.nl/courses/microelectronics/solar-cells/readings/, 4.3 (visited 15-3-14)

[10] A. Sahay, V.K. Sethi, A.C. Tiwari, *A comparative study of attributes of thin films and crystalline photovoltaic cells*, VSRDIJMCAPE **3**, 268-269 (2013)

[11] F. Priolo, *Silicon nanostructures for photonics and photovoltaics*, nature nanotech. **9**, 26 (2014)

[12] M.A. Green*, Thin-film solar cells: review of materials, technologies and commercial status*, J Mater Sci: Mater Electron **18,** 16 **(**2007)

[13] W.A. Badawy, *A review on solar cells from Si-single crystals to porous materials and quantum dots*, Journ. Of Adv. Research, 3-4 (2013)

[14] A. M. Smith, S. Dave, S. Nie, L. True, X. Gao, *Multicolor quantum dots for molecular diagnostics for cancer,* Expert Rev. Mol. Diagn. **6** (2), 232 (2006)

[15] A. M. Smith, S. Dave, S. Nie, L. True, X. Gao, *Multicolor quantum dots for molecular diagnostics for cancer*, Expert Rev. Mol. Diagn. **6** (2), 232 (2006)

[16] Figure taken from: Quantum dots, http://www.sigmaaldrich.com/materials-science/nanomaterials/quantum-dots.html, visited on 6-3-2014

[17] Waheed A. Badaway*, A review on solar cells from Si-single crystals to porous materials and quantum dots*, Journ. Of Adv. Research, 3-4 (2013)

[18] S. N. Agbo, Growth and Characterization of Thin Film Nanocrystalline silicon Materials and Solar cells, P.h.d. Thesis, Technical University Delft, 4 (2012)

[19] S. N. Agbo, Growth and Characterization of Thin Film Nanocrystalline silicon Materials and Solar cells, P.h.d. Thesis, Technical University Delft, 4 (2012)

[20] M. Kondo, A. Matsuda, *Novel aspects in thin film silicon solar cells-amorphous, microcrystalline and nanocrystalline silicon*, Thin Solid Films **457**, 98 (2004)

[21] S. N. Agbo, *Growth and Characterization of Thin Film Nanocrystalline silicon Materials and Solar cells*, P.h.d. Thesis, Technical University Delft, 5+10 (2012)

[22] L. Kroely, *Process and material challenges in the high rate deposition of microcrystalline silicon thin films and solar cells by Matrix Distributed Electron Cyclotron Resonance plasma*, Ph.D thesis (final version), Université Mentouri Constantine (UMC), 83-85 (24-12-2010)

[23] A.V. Shah, J. Meier, E. Vallat-Sauvain, N. Wyrsch, U. Kroll, C. Droz, U. Graf, *Material and solar cell research in microcrystalline silicon,* Solar En. Mat. And sol. Cells **78**, 6 (2003)

[24] A.V. Shah, J. Meier, E. Vallat-Sauvain, N. Wyrsch, U. Kroll, C. Droz, U. Graf, *Material and solar cell research in microcrystalline silicon,* Solar En. Mat. And sol. Cells **78**, 8-9 (2003)

[25] B. Delley, E.F. Steigmeiser, *Quantum confinement in Si nanocrystals,* Physical Review B **47**, 46 (1993)

[26] G. Conibeer, I. Perez-Wurfl, X. Hao, D. Di, D. Lin, *Si solid-state of quantum dot-based materials for tandem solar cells*, Nanosc. Res. Lett. **7:**193, 1 (2012)

[27] K. Dohnalová et al., *Surface brightens up Si quantum dots: direct bandgap-like size-tunable emissions*, Light: Sicence & Applications **2**, 1 (2013)

[28] F. Priolo, *Silicon nanostructures for photonics and photovoltaics*, nature nanotech. **9**, 21 (2014)

[29] N. Sircar & D. Bougeard, *Experimental investigation of the optical spin selection rules in bulk Si and Ge/Si quantum dots*, Phys. Rev. B **89**, 1 (2014)

[30] A. Vivas Hernandez, T.V. Torchynska, A.L. Quintos Vazquez, Yasuhiro Matsumoto, L. Khomenkova, L. Shcherbina, *Emission and structure investigations of Si nano-crystals in amorphous silicon,* J. of Physics: Conf. Series **61**,1233 (2007)

[31] W. A. Su, W. Z. Shen, *A statistical exploration of multiple exciton generation in silicon quantum dots and optoelectronic application,* Appl. Phys. Lett. **100**, 071111-3 (2012).

[32] G. Conibeer, I. Perez-Wurfl, X. Hao, D. Di, D. Lin, *Si solid-state of quantum dot-based materials for tandem solar cells*, Nanosc. Res. Lett. **7:**193, 1 (2012)

[33] Figure taken from: Research Cell Efficiency Records, http://www.nrel.gov/ncpv/ (date visited 6-3-2014)

[34] A. Turkin et al., *On the evolution of nanocluster size distribution in a nanocluster aggregation source*, Journal of appl. Phys. **111**, 1 (2012)

[35] Y. Yamamura, H Tawara, *Energy dependence of ion-induced sputtering yields from monatomic solids at normal incidence*, Atom. Data and Nucl. Data Tables Vol. 62, 151 (1996)

[36] Oxford Applied Research, NC200U-B RF/DC Nanocluster source manual, Thin film deposition solutions, 4

[37] S. Swann, *Magnetron sputtering*, Phys. Technol. **19**, 68 (1998)

[38] S. Swann, *Magnetron sputtering*, 69

[39] S. Swann, *Magnetron sputtering*, 70

[40] S. Swann, *Magnetron sputtering*, 73

[41] http://www.oaresearch.co.uk, Products, nanocluster solutions, Nanocluster Source, Application Data, figure 2 (25-3-14)

[42] http://www.oaresearch.co.uk, Products, nanocluster solutions, Nanocluster Source, Application Data (25-3-14)

[43] T. Miyasato, M. Tonouchi, *Preparation of compound semiconductor films by means of hydrogen plasma sputtering*, Mat. Sci. and Engi. **B9**, 195 (1991)

[44] D. W. Hahn, *Raman scattering theory*, 1-3+7-8 (2007). Taken from:http://plaza.ufl.edu/dwhahn/Diagnostic%20Tutorials.html, date visited 26-3-2014.

[45] Figure taken from: www.americanlaboratory.com, Articles: *Rapid characterization of large Areas of Graphene using Raman Spectroscopy,* date visited 27-3-2014

[46] D. W. Hahn, *Raman scattering theory*, 8-9 (2007). Taken from: http://plaza.ufl.edu/dwhahn/Diagnostic%20Tutorials.html, date visited 26-3-2014.

[47] H. Hwang, M. G. Park, H. Ruh, H. Yu, *Investigations on Microcrystalline Silicon Films for Solar Cell Application,* Bull. Korean Chem. Soc. **31**, 2910-2911 (2010)

[48] Image taken from: http://www.ptbsales.com/semiconductor/veeco/dektak8.html, date visited 9-7-2014

[49] W. Jacob, A. Keudell, T. Schwarz-Selinger, *Infrared Analysis of Thin films: Amorphous, Hydrogenated Carbon on Silicon,* Braz. Jour. Of Phys. **30**, 510 (2000)

[50] T. Owen, *Fundamentals of UV-visible spectroscopy,* 12-14+25-26, taken from: http://www.chem.agilent.com/Library/primers/Public/5980-1398E.pdf, date visited 28-3-2014

[51] M.Y Nadeem, W. Ahmed, *Optical properties of ZnS Thin* Films, Turk J Phy 24, 653 (2000)

[52] J. Dharma, A. Pissal, *Simple Method of Measuring the Band Gap Energy Value of TiO_2 in the Powder Form using a UV/Vis/NIR spectrometer,* PerkinElmer Application Note, 2009.

[53] A.B. Murphy, *Band-gap determination from diffuse reflectance measurements of semiconductor films, and application to photo electrochemical water-splitting*, Sol. En. Mat. & Sol. Cells **91**,1134 (2007)

[54] P. E. West, *Introduction to Atomics Force Microscopy Theory Practice Applications,* p. 1-2 taken from: http://bitc2-preview.sr.unh.edu/TRC/REFERENCES/AFM/AFM_TheoryPracticeApplications_TEXT.pdf, date visited 31-3-2014

[55] R. A. Wilson, H. A. Bullen, *Introduction to Scanning Probe Microsccopy (SPM), Basic theory Atomic Force (AFM),* p. 2. Found on: http://asdlib.org/onlineArticles/ecourseware/Bullen/SPMAFMTheory.htm, date visited 31-3-2014.

[56] R. A. Wilson, H. A. Bullen, *Introduction to Scanning Probe Microsccopy (SPM), Basic theory Atomic Force (AFM),* p. 4-5.

[57] P. E. West, *Introduction to Atomics Force Microscopy Theory Practice Applications,* p. 23 http://bitc2-preview.sr.unh.edu/TRC/REFERENCES/AFM/AFM_TheoryPracticeApplications_TEXT.pdf, date visited 31-3-2014

[58] R. A. Wilson, H. A. Bullen, *Introduction to Scanning Probe Microsccopy (SPM), Basic theory Atomic Force (AFM),* p. 5.

[59] P. E. West, *Introduction to Atomics Force Microscopy Theory Practice Applications,* p. 3+33. http://bitc2-preview.sr.unh.edu/TRC/REFERENCES/AFM/AFM_TheoryPracticeApplications_TEXT.pdf, date visited 31-3-2014

[60] R. A. Wilson, H. A. Bullen, *Introduction to Scanning Probe Microsccopy (SPM), Basic theory Atomic Force (AFM),* p. 7.

[61] Image taken from: http://www.bioimaging-utrecht.nl/equipment/uu-biology/8-equipment/7-tecnai-10.html, date visited 4-2014

[62] Image taken from: http://pmvz-esteem.cemes.fr/index.php/transnational-access/infrastructures-and-installations/delft, date visited 4-2014

[63] S. Hayashi, K. Yamamoto, *Optical properties of Si-rich SiO2 films in relation with embedded SI mesoscopic particles*, J. of Lumi. **70**, 355 (1996)

[64] S. Hayashi, K. Yamamoto, *Optical properties of Si-rich SiO2 films in relation with embedded SI mesoscopic particles*, J. of Lumi. **70**, 356 (1996)

[65] Data taken from: http://www.tue.nl/universiteit/faculteiten/faculteit-tn/onderzoek/onderzoekscluster-plasmas-en-straling/plasma-and-materials-processing-pmp/research-topics/microcrystalline-silicon-for-thin-film-solar-cells/, date visited: 2-5-2014

[66] Data taken from: http://www.superstrate.net/pv/amorphous/defect-measurement.html, date visited 3-5-2014

[67] Data set taken from Excel sheet found on: http://www.pveducation.org/pvcdrom/materials/optical-properties-of-silicon, date visited:2-5-2014

[68] N. M. Abdul-Meer, M. C. Abdulrida, *Direct Optical Energy Gap in Amorphous Silicon Quantum Dots*, Journal of Modern Physics **2,** 1530 (2011)

[69] J.K. Rath, *Micro-/Poly-crystalline silicon materials for thin film photovoltaic devices: Physical properties,* Photovolt. And Photoact. Mat. – Propert. and Appl., 171

[70] C. Palsule, et al., *Fast photoluminescence decay in a-SI,* Phys. Rev. B **47**, 9309 (1993)

[71] J.M. Zuo and J.C. Mabon, Web-based Electron Microscopy Application Software: Web-EMAPS, Microsc Microanal 10(Suppl 2), 2004. Found on: http://emaps.mrl.uiuc.edu/

[72] P. Jensen, A. Clément, L. J. Lewis, *Diffusion of nanoclusters*, Computational Materials Science **30,** 140 (2004)